RETRIEVING VEGETATION PHENOLOGY WITH PLANETSCOPE IMAGES FOR A SEMI-ARID RANGELAND IN KENYA

YAN CHENG
FEBRUARY, 2019

SUPERVISORS:
Dr. A. Vrieling
Dr. M. Marshall

RETRIEVING VEGETATION PHENOLOGY WITH PLANETSCOPE IMAGES FOR A SEMI-ARID RANGELAND IN KENYA

YAN CHENG
Enschede, The Netherlands, February, 2019

Thesis submitted to the Faculty of Geo-Information Science and Earth Observation of the University of Twente in partial fulfilment of the requirements for the degree of Master of Science in Geo-information Science and Earth Observation.
Specialization: Natural Resources Management

SUPERVISORS:
Dr. A. Vrieling
Dr. M. Marshall

THESIS ASSESSMENT BOARD:
Dr. A. Nelson (Chair)
Dr. F. Fava (External Examiner, International Livestock Research Institute)

ABSTRACT

Vegetation phenology refers to the time of periodic events in vegetation life cycles, such as the start of green-up and flowering. For semi-arid rangelands, where the cloud cover is persistent during rainy seasons and vegetation life cycles are relatively short (approximately three to four months), satellite-based phenology monitoring requires temporally dense images. Moreover, fine-resolution images can provide more spatial details for heterogeneous landscapes. PlanetScope (PS) is a promising constellation that provides daily global observations at 3m resolution with about 170 CubeSats (small satellites), and as such may have more options to provide more frequent optical cloud-free imagery with finer spatial resolution as compared to other satellites like Sentinel-2 or Landsat. The objective of this study is to evaluate the potential of PS imagery for retrieving vegetation phenology in semi-arid rangelands in comparison to alternative data sources, including RGB field camera photography, Sentinel-2 images, and MODIS images. The study area is a semi-arid rangeland site in Kenya, where the dominant vegetation communities are open grass, shrubs, mixed shrubs and grass, and trees with understory grass. Before phenology estimation, the clouds and cloud shadows in PS images were detected based on a monthly threshold-based decision tree. The overall accuracy of the cloud and cloud shadow detection was 83.63%. Four phenological metrics, i.e., the start of season (SOS), end of season (EOS), maximum vegetation index value, and integral vegetation index from the start of season to the end of season, were then retrieved from satellite-based NDVI and camera-based greenness chromatic coordinate time series after fitting to a double hyperbolic tangent model. PS-derived SOS and EOS were on average within eight days and 15 days of camera-derived SOS and EOS. Due to higher temporal resolution (~daily), there was a better density of cloud-free observations in PS-based NDVI time series than Sentinel-2-based NDVI time series, as a consequence of which PS-based phenology retrievals were less impacted by the persistent clouds during rainy seasons. Moreover, due to the finer spatial resolution (3m), PS-derived phenology maps showed more spatial details than phenology maps derived from commonly used coarse-resolution sensors like MODIS. Overall, the results demonstrate the potential of using PS images for fine-scale phenology analysis in semi-arid rangelands. The spatially-detailed vegetation phenology derived from PS at the local scale can provide useful input for understanding the response of semi-arid rangelands to environmental factors. Further investigation of using PS images as supplementary and/or validation data for the phenology analysis base on other free satellite datasets, such as Sentinel-2, can be a way of using PS images for the analysis of vegetation phenology at the global scale.

Keywords: NDVI time series, CubeSat, cloud and cloud shadow detection, Sentinel-2, MODIS, digital repeat photography

ACKNOWLEDGEMENTS

I would like to thank my supervisors, Dr Anton Vrieling and Dr Michael Marshall. They were really instrumental during the conceptualization of my research from proposal writing until thesis writing phase. There are not enough words to express how grateful I am for their unconditional help!

I would also like to thank Dr Francesco Fava and other staffs in the International Livestock Research Institute (ILRI) for their assistance during the fieldwork in Nairobi, Kenya.

To ITC Excellence Scholarship Programme, thanks for providing me an opportunity to peruse MSc in the Netherlands.

Last but not least, I want to thank my friends, my boyfriend Marcius Elaeo Isip and my parents for always supporting me.

TABLE OF CONTENTS

LIST OF FIGURES

LIST OF TABLES

LIST OF APPENDIX

LIST OF ABBREVIATIONS

ASALs	Arid or Semi-Arid Lands
AVHRR	Advanced Very High Resolution Radiometer
b2_savg	Sum average of reflectance in Band 2
cumNDVI	Accumulation of VI between SOS and EOS
DOY	Day of Year
EOS	The date of the end of season
ETM	Enhanced Thematic Mapper
EVI	Enhanced Vegetation Index
GCC	Greenness Chromatic Coordinate
GCC90	The 90th percentile of all GCC values within the three-day window
GLCM	Gray Level Co-occurrence Matrix
LR2017	Long rain season in 2017 (1 March 2017 – 1 October 2017)
LR2018	Long rain season in 2018 (1 February 2018 – 1 October 2018)
maxGap	Maximum difference (days) between two successive observations
maxNDVI	Maximum NDVI in the fitted curve
MODIS	Moderate Resolution Imaging Spectroradiometer
MSD	Mean Signed Deviation (Bias)
NDVI	Normalized Difference Vegetation Index
$NDVI_P$, $NDVI_S$, $NDVI_M$	NDVI time series derived from PS, Sentinel-2 and MODIS
nImages	The average number of cloud-free observations
NIR	Near-infrared
r	Pearson's Correlation Coefficient
RF	Random Forest
RMSD	Root Mean Squared Deviation
ROI	Region of Interest
PS	PlanetScope
SOS	The date of the start of season
SR2017	Short rain season in 2017（1 September 2017 – 1 March 2018)
SWIR	Short-wavelength infrared
VI	Vegetation index

1. INTRODUCTION

1.1. Background

Rangelands cover about 40% of the global land area and play an essential role in the global sustainability by providing foods and habitats to wildlife and livestock (Reeves et al., 2014). Vegetation productivity of rangelands strongly relates to temperature and precipitation, both of which influence the water availability for plants (Ouled Belgacem & Louhaichi, 2013). In the arid or semi-arid lands (ASALs), such as in Eastern Africa, the rangeland dynamics are sensitive to rainfall variability (Grossiord et al., 2017; Hovenden et al., 2004). Many climate change projections in Eastern Africa show that temperatures will continue to increase and rainfall will become more variable, leading to more frequent and intense extreme events, such as droughts and floods (IPCC, 2013). To improve the resilience of rangeland ecosystems and prevent the loss of livestock caused by drought-driven forage scarcity, the monitoring of rangeland dynamics in ASALs is very important. Vegetation phenology is an essential element of rangeland dynamics.

Vegetation phenology refers to the time of different stages in plant life cycles, such as sprouting, flowering, and ripening (Schwartz, 2013). Most phenology studies in rangelands aim to understand how climate change will impact changes in vegetation phenology. Climate drivers such as elevated atmospheric CO_2 concentration (Zelikova c, 2015; Hovenden et al., 2008), temperature (Shen et al., 2011; Yu et al., 2003), precipitation (Prevéy & Seastedt, 2014; Shen et al., 2011), and extreme climate events (Jentsch et al., 2009) have been found to strongly relate to early green-up and flowering. Other studies predict phenological shifts and changes in rangeland productivity under projected climate change (Chang et al., 2017; Hermance et al., 2015; Bloor et al., 2010). For the semi-arid rangelands in Eastern Africa, no spatially and temporally detailed phenology assessments have been performed at the landscape scale. As a result, the phenological variations of different vegetation communities as a response to rainfall variability are still poorly understood (Cho et al., 2017; Dahlin et al., 2017).

The traditional method used to monitor vegetation phenology relies on human observations. However, observers can only visually inspect distinct phenological phases such as flowering (Sparks & Menzel, 2002). Vegetation indexes (VIs) are a straight-forward quantifiable measure of vegetation growth status, and can serve as an alternative method to retrieve threshold-based phenological metrics, such as the start of season (SOS) and the end of season (EOS) (Vrieling et al., 2017; Zhang et al., 2014; Keenan et al., 2014). VI time series can be generated from multi-temporal optical images, as obtained by field cameras or satellite platforms (Adole et al., 2016).

Digital repeat photography (Richardson et al., 2007) refers to the ground-based method for collecting multi-temporal optical images. Digital cameras with at least three channels (i.e., red, green, blue) are installed at fixed positions in the field and take one or more pictures every day. Resulting photograph series are a substitute for direct field observations by humans. In addition, they can be used to calculate canopy greenness from RGB values followed by retrieving phenological metrics (Crimmins & Crimmins, 2008; Richardson et al., 2007; Abu-Asab et al., 2001). Digital repeat photography has been widely used for phenology assessment of forest systems (Keenan et al., 2014) and grassland systems (Inoue et al., 2015). However, to monitor vegetation phenology at the landscape scale with digital repeat photography, a large number of cameras would be required, which may not be the most cost- and time-efficient option.

Satellite-based remote sensing provides a cost-effective method to retrieve vegetation phenology at the landscape scale (Guan et al., 2014). Given the requirement of frequent observations on vegetation phenology monitoring, most satellite-based phenology studies used coarse-resolution images captured by sensors with a daily revisit time, such as the Moderate Resolution Imaging Spectroradiometer (MODIS) (250 m – 500m) (Gong et al., 2015) and the Advanced Very High Resolution Radiometer (AVHRR) (1km) (Jolly & Running, 2004). However, in most cases, vegetation cover is spatially heterogeneous, resulting in multiple vegetation species in a single image pixel. Therefore, coarse-resolution images are not effective for extracting phenological metrics at species-level for heterogeneous land covers (Vrieling et al., 2018), such as semi-arid rangelands in East Africa that are characterized by a mixture of woodland and grassland. Fine-resolution images (≤30 m) may provide a better data source for this purpose.

The main problem in using fine-resolution images is the long revisit time. For example, the revisit time of Landsat-8 is 16 days. This can lead to an insufficient number of cloud-free observations to accurately represent the within-season vegetation dynamics, especially in tropical areas with persistent cloud cover. To solve this problem, Fisher et al. (2006) proposed to combine Landsat imagery of multiple years to create a single synthetic year. This method can be used to retrieve an average phenology over multiple years, which can subsequently be adjusted by observations of a specific year to estimate phenological metrics for that year (Melaas et al., 2016; Melaas et al., 2013). However, this method requires a reasonably stable phenology from year to year. Therefore, for semi-arid rangelands in Eastern Africa with significant annual variations in phenology, multi-year data integration is not a good option (Gachoki, 2018). To retrieve single year vegetation phenology at fine resolution, 10m resolution Sentinel-2 images with a relatively short revisit time of ~5 days have been used for a Dutch barrier island where vegetation has a long annual cycle (Vrieling et al., 2018). In the semi-arid rangelands of Eastern Africa vegetation has shorter greening cycles and significant cloud cover during parts of the year (Gachoki, 2018), which may require a shorter revisit time to accurately describe the seasonal changes of vegetation.

PlanetScope (PS) images (Planet Team, 2017) could provide a potential alternative to Sentinel-2 images. PS images are captured by the PS constellation, which consists of approximately 170 4-kg CubeSats (small satellites). Due to the large number of CubeSats in the same orbit, the constellation achieves a short revisit time (~1 day), which possibly allow for temporally denser observations than Sentinel-2 particularly during months of relatively persistent cloud cover. The high spatial resolution of PS images (3m) may allow for assessing phenology at the species level. However, because the launch of the CubeSats in PS constellation started in 2013 and its data are commercially available with limited free availability for research purposes, none of the existing studies that use these data is related to phenology. Cooley et al. (2017) used PS images to generate a VI time series to determine changes in dynamic surface water on the Yukon Flats. They discussed an important limitation of the application of PS images, which is the lack of an applicable cloud and cloud shadow mask products and automated cloud and cloud shadow detection algorithms. Effective masking is needed however to avoid using contaminated vegetation index values that do not relate to the vegetation status when estimating phenology (Champion, 2016; Tseng et al., 2008).

1.2. Research questions

The main aim of this study is to evaluate the utility of PS images for retrieving vegetation phenology for semi-arid rangelands in Eastern Africa. To achieve this aim, the research objectives and linked research questions are as follows:

(1) to develop and assess a cloud and cloud shadow screening algorithm for PS images;
Q1.1. What is the accuracy of the cloud and cloud shadow detection algorithm?

(2) to assess if PS images can be used to accurately retrieve phenological metrics;
Q2.1. What is the accuracy of PS-derived phenological metrics when compared to camera-derived ones at the camera locations?
Q2.2. What is the influence of image availability of PS on the accuracy of phenological metrics?

(3) to map the vegetation phenology derived from PS images and to analyse spatial and temporal patterns;
Q3.1. Are there any spatial artefacts on PS-derived phenology maps? If yes, what causes those artefacts?
Q3.2. Do different vegetation communities show significant differences in vegetation phenology?
Q3.3. Do these differences vary across different seasons?

(4) to compare PS-derived phenological metrics with Sentinel-2- and MODIS-derived ones.
Q4.1. What is the difference in the temporal density of cloud-free observations between PS and the other two satellite images?
Q4.2. Is the accuracy of PS-derived phenological metrics higher than Sentinel-2- and MODIS- derived ones when both compared to phenological metrics derived from field camera photographs?

2. STUDY AREA

More than 80% of the Kenya land area is rangeland, providing important natural resources to wildlife, livestock, and millions of pastoralists and agro-pastoralists (Mathu, 2009). Most of these rangelands are located on ASALs, which are vulnerable to recurring droughts. Kapiti Farm is a semi-arid rangeland site in southern Kenya. It is owned by the International Livestock Research Institute (ILRI) and used as a research station to conduct research on sustainable livestock and rangeland management. The farm covers approximately 128 km^2 and is located in the south of Machakos County (*Figure 1*). On the farm, about 2,500 head of beef cattle, 1,200 sheep, and 250 goats are maintained by 80 ILRI staffs for research purposes. As one of the few rangelands without serious landscape fragmentation in Kenya, it also serves as an important habitat for large numbers of wildlife. The wild animals in Amboseli National Park regard Kapiti Farm as a transitory territory during the rain seasons. Taking advantage of location, Kapiti Farm is also a critical ecological corridor for the migration of mammals (International Livestock Research Institute (ILRI), 2018).

Based on a field survey conducted by Gachoki (2018) in 2017, the dominant vegetation communities in Kapiti Farm are open grass, Acacia shrubs, mixed shrubs, and trees. In general, there are two wet seasons in a year. Based on *in-situ* records of daily precipitation from 1 January 2001 to 3 October 2018 (*Figure 2*), the "short rain" (SR) season is approximately from October to January and the "long rain" (LR) season is approximately from March to June. The average precipitation during the last 18 years (2001-2018) is 195.60 mm for SR and 252.72 mm for LR. Precipitation characteristics and grazing intensity are the most important controls on the dynamics of vegetation life cycle and productivity in Kapiti Farm. The seasonal vegetation responds therefore strongly to the timing and quantity of rainfall.

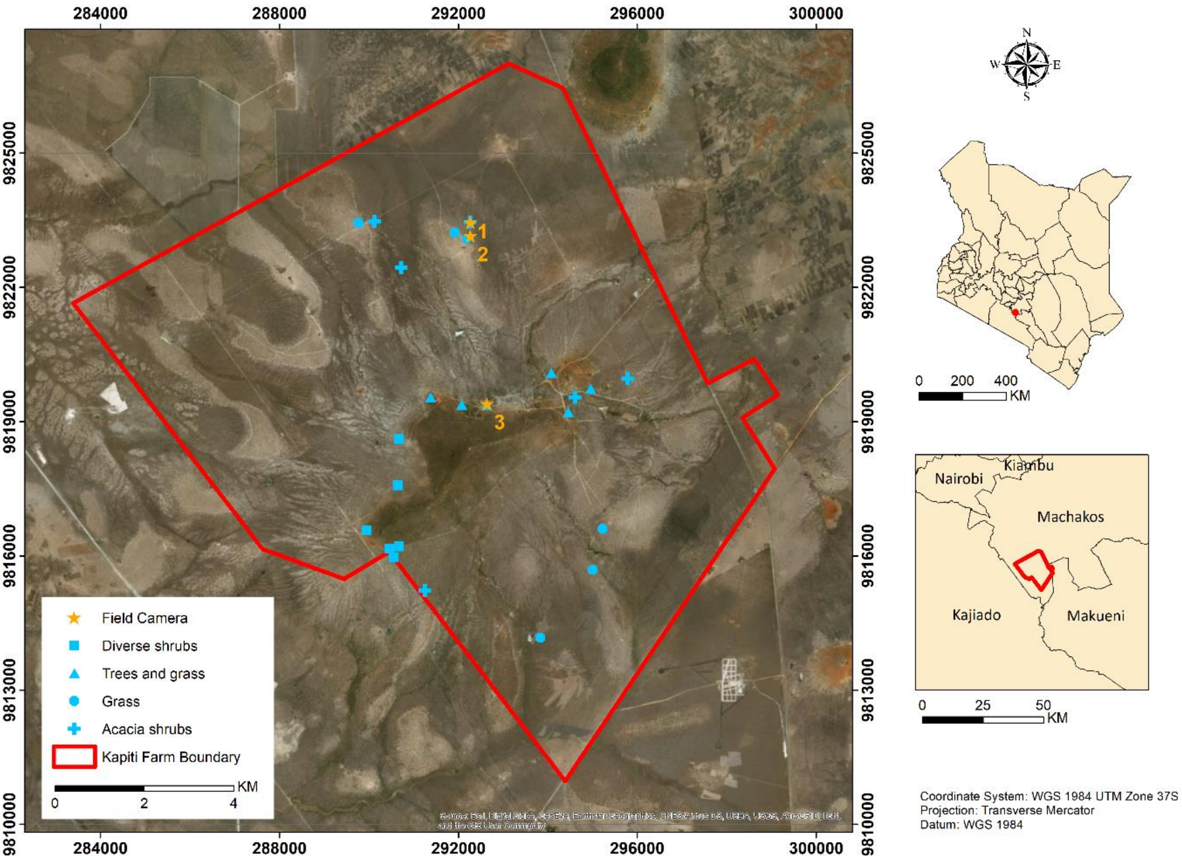

Figure 1: Overview of the study area. The background image is a WorldView-2 scene (0.5m) acquired on 2 February 2017 provided by Digital Globe.

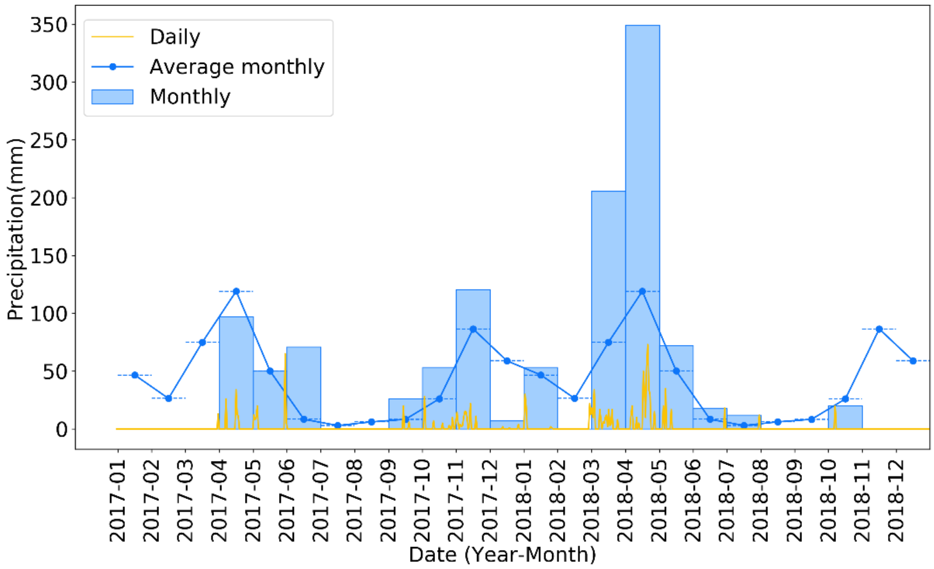

Figure 2: Precipitation characteristics in Kapiti Farm based on manual in-situ daily rain gauge data. Daily and monthly precipitation are shown from 1 January 2017 to 3 October 2018. The average monthly precipitation was calculated based on precipitation in the past 18 years (January 2001- October 2018).

3. DATA

Four sources of optical images were used in this study, i.e., digital repeat field camera photographs, PS, Sentinel-2, and MODIS images. Camera photographs were used to understand vegetation dynamics at the vegetation community level. Moreover, the camera-derived phenological metrics were used as a form of *in-situ* measurements to evaluate satellite-derived phenological metrics and to assess if important changes in greenness may be missed by satellites. PS, Sentinel-2, and MODIS images were used to retrieve phenological metrics for the entire study area and to analyse the influence of spatial and temporal resolution on the estimates of phenological metrics. Vegetation survey and precipitation records collected in Kapiti Farm were used to analyse the potential environmental driving forces of phenological variations. Due to data availability, the timeframe considered in this study is from 1 March 2017 to 1 October 2018, which covers three rain seasons and is related to three vegetation seasons: 1 March 2017 – 1 October 2017 (named LR2017), 1 September 2017 – 1 March 2018 (SR2017), 1 February 2018 – 1 October 2018 (LR2018). *Table 1* shows an overview of the datasets used in this study.

Table 1: Overview of datasets

	Acquisition time	**Resolution (m)**	**Revisit time (days)**	**Cloud mask? (Yes/No)**
Optical images				
PlanetScope (Analytic Ortho Scene)	3/3/2017 – 1/10/2018 (LR2017, SR2017 and LR2018)	3	1	No
Sentinel-2 (Sentinel-2A, Sentinel-2B)	6/9/2017 - 1/10/2018 (SR2017 and LR2018)	10	5	Yes
MODIS (MOD13Q1, MYD13Q1)	6/3/2017 – 1/10/2018 (LR2017, SR2017 and LR2018)	250	1	Yes
Camera photos	5/10/2017 to 1/10/2018 (SR2017 and LR2018)			
Other datasets				
Vegetation samples	Collected in October 2017			
Daily Precipitation records	1/1/2001 to 31/10/2018			

3.1. PlanetScope-derived NDVI time series

PS is a satellite constellation consisting of 170+ CubeSats (small satellites) operated by Planet Labs (Houborg & McCabe, 2018). The number of CubeSats in this constellation is still increasing. The majority of CubeSats are in a sun-synchronous orbit with an equator crossing time between 9:30 and 11:30 (local solar time) (Planet Team, 2017). Other CubeSats are in the International Space Station orbit with a varying equator crossing time. The inconsistent acquisition time in a day may result in variations in VI time series that are not due to changes in the land surface (Houborg & McCabe, 2018). With all CubeSats combined, the PS constellation is able to capture more than 346 million km^2 of land surface every day. PS images have four spectral bands, i.e. blue (455 – 515 nm), green (500 – 590 nm), red (590 – 670 nm) and near-infrared (NIR) (780–860 nm). The spatial resolution is 3 m, which is resampled from 3.5 m – 4 m nadir sample distance using a Cubic Convolution resampling kernel.

Planet Labs provides three types of PS products corresponding to three different pre-processing levels. The product used in this study is the PS Analytic Ortho Scene Product (Surface reflectance product), for which the 4-band image (GeoTIFF format) has been geometrically and atmospherically corrected. After the geometric correction, the positional accuracy of these images is less than 10 m Root Mean Square Error (RMSE). The atmospheric correction is based on the 6S radiative transfer model with ancillary data from MODIS (Planet Team, 2017). The image quality is indicated in an XML metadata file. The images with sun altitude greater than or equal to 10 degrees, off-nadir view angle less than 20 degrees and saturated pixels fewer than 20% are classified as good quality (Planet Team, 2017). Apart from 4-band image files and XML metadata, each PS product also contains an Unusable Data Mask (UDM). The UDM only provides a very rough cloud mask, and was deemed not useful for this study.

A total of 460 PS Analytic Ortho Scene products between 3 March 2017 and 1 October 2017 were downloaded from Planet Explorer (Planet Labs Inc., 2018). Images with bad quality as indicated in the corresponding XML metadata file were excluded from the database. PS images acquired in the same day from the same orbit were merged and clipped to the study area extent. This resulted in 208 merged PS images. The normalized difference vegetation index (NDVI) was then calculated for each PS image. In satellite-based phenology studies, the NDVI and enhanced vegetation index (EVI) are the two most commonly-used VIs. In high biomass areas, such as dense forests, EVI has a better performance as compared to NDVI, because the signal saturates less quickly (Huete et al., 2002). In low biomass areas, such as semi-arid rangelands, the saturation effect of NDVI is not a major issue and NDVI can show a broader dynamic range than EVI (Huete et al., 2002). However, NDVI is sensitive to wet versus dry soil (Huete et al., 2002), which may impact on the change detection of vegetation greenness. Nevertheless, in this study, it was chosen to focus on using NDVI to assess vegetation dynamics for Kapiti Farm. The PS-derived NDVI time series are named in this thesis as $NDVI_P$ (the subscript P referring to PS).

3.2. Sentinel-2-derived NDVI time series

The Sentinel-2 mission consists of two satellites, Sentinel-2A and Sentinel-2B, which were launched on 23 June 2015 and 7 March 2017, respectively. They are in the same orbit with similar zenith angles (5.2 vs 7.8°) and opposite azimuth angles (104.4 vs 288.6°). With two satellites, Sentinel-2 can revisit the same point on the earth surface in five days with the same observation geometry. The revisit time is less than five days towards the poles where satellite orbits overlap, but this is not the case for Kapiti Farm. Sentinel-2 images have 13 bands, of which four bands have a 10 m resolution, i.e. blue (492 – 558 nm), green (559 – 595 mm), red (664 – 695 nm), and NIR (832 – 938 nm).

All 62 Level-1B products (tile code 37MBU) were downloaded from the Copernicus Open Access Hub (European Space Agency (ESA), 2018). There are no available Sentinel-2B images before June 2017 for Kapiti Farm, and because of the limited amount of Sentinel-2A images for LR 2017, Sentinel-2-based phenology analysis focussed only on the period 6 September 2017 to 1 October 2018, i.e. covering only SR2017 and LR2018. The Level-1B products were atmospherically corrected using the Sen2Cor processor (version 2.5.5). One of the outputs from Sen2Cor is a scene classification file; pixels classified as cloud shadow, cloud, and thin cirrus were masked. In addition, to filter out cloud shadows that are not included in the scene classification file, pixels with less than 0.01 reflectance in the blue band were also masked out.

The NDVI was then calculated for each Sentinel-2 image. The Sentinel-2-derived NDVI time series are named in this thesis as $NDVI_S$ (the subscript S referring to Sentinel-2).

3.3. MODIS-derived NDVI time series

MOD13Q1 and MYD13Q1 Version 6 250m resolution vegetation index products (Didan, 2015a; Didan, 2015b) were accessed through Google Earth Engine (GEE). MOD13Q1 and MYD13Q1 were generated using atmospherically corrected images from MODIS/Terra and MODIS/Aqua satellite. Each product includes 16-day composite NDVI and EVI. There is an 8-day shift between MOD13Q1 and MYD13Q1, so the combination of these two products results in an average eight-day interval for the combined VI time series. The information of quality reliability and acquisition time of each pixel are also given along with NDVI and EVI layers. In this research, only the NDVI layer was used and pixels flagged as poor observations (code 3 and 4) were removed from the NDVI time series. The MODIS-derived NDVI time series are named in this thesis as $NDVI_M$ (the subscript M referring to MODIS).

3.4. Field camera photos

To monitor the vegetation phenology, three Bushnell Trophy Cam Essential (model 119736) trail cameras (with identifiers KE01, KE02, KE03) were installed in Kapiti Farm (*Figure 1*) in October 2017. *Table A1* in the Appendix shows the basic information about the three camera locations. Each of these three cameras is set up to take one RGB photo (JPG format) every 30 minutes from 8:00 to 17:30 using Eastern Africa Time (EAT). *Table A2* in Appendix shows the properties of cameras and photographs. *Figure 3* shows sample photos captured by each camera.

Camera photos captured between 5 October 2017 and 1 October 2018 were used in this study. The photos that are blurred, overexposed or underexposed, or covered by non-vegetated obstructions (e.g. animals) were visually identified and discarded from the database. Subsequently, VI time series were generated from the camera photo series. One of the commonly-used VIs in camera-based phenology studies is Greenness Chromatic Coordinate (GCC) (Migliavacca et al., 2011; Richardson et al., 2007). It is calculated by dividing the brightness of the green channel by the sum of brightness of the red, green and blue channels (Eq. 1) (Gillespie et al., 1987). This nonlinear transformation can mitigate the influence of scene illumination on the brightness levels (Sonnentag et al., 2012; Woebbecke et al., 1995; Gillespie et al., 1987).

$$GCC = \frac{Green}{Red + Green + Blue} \tag{1}$$

To generate GCC time series for camera photos, the average GCC value within a region of interest (ROI) was calculated for each photograph. *Figure 3* shows the ROIs in the field of view of each camera. Each ROI represents a dominant vegetation community or the same vegetation community in a different condition. For example, ROI1 in camera frame KE01 (KE01-1) represents open grass. KE02-1 and KE02-2 represent shrubs and grasses, KE03-1, KE03-2 and KE03-3 represent tree canopy, grass under the tree and grass. In the case of more than one vegetation community in the field of view, such as for camera KE02 and KE03, another ROI that contain most of the field of view (KE02-0 and KE03-0) was also created to represent the mixture of multiple vegetation communities as would be also observed from a satellite view. To further reduce the influence of different scene illumination on GCC, the 90^{th} percentile of all GCC values within a non-overlapping three-day window (GCC90) was extracted and assigned to the centre day. This moving-window approach for generating GCC time series was proposed by Sonnentag et al. (2012).

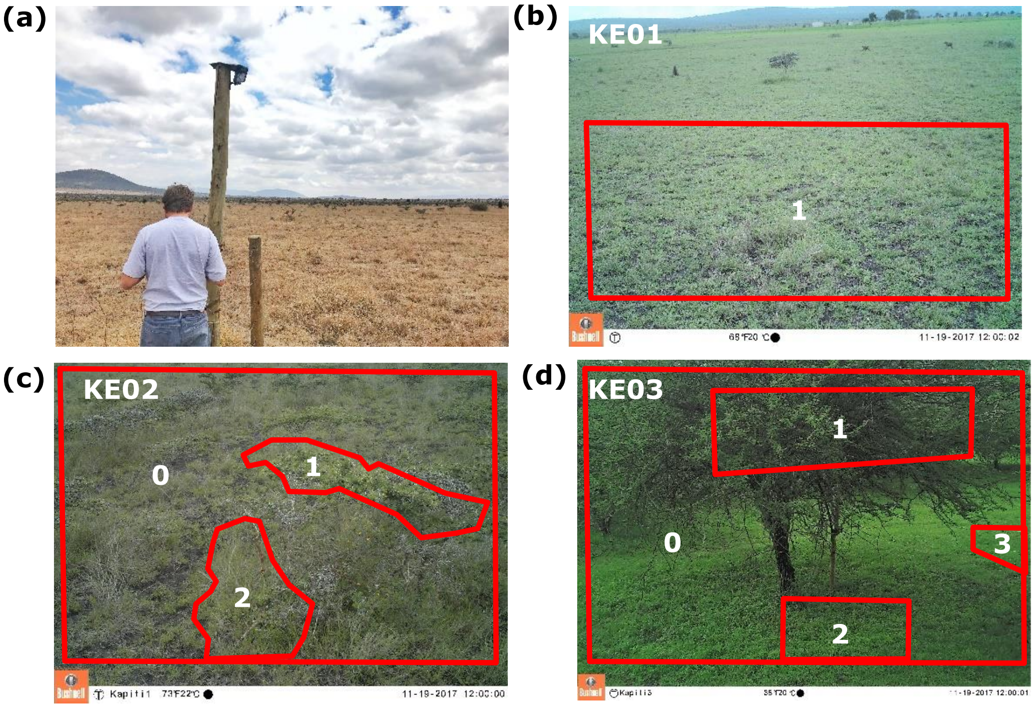

Figure 3: Sample photos taken by the three cameras in Kapiti Farm. (a) the installation of field cameras in Kapiti Farm. (b) – (d) sample photos taken by cameras KE01, KE02, and KE03 at 12:00 on 19 November 2017. The red polygons in b-d indicate the region of interest (ROI) used for extracting averaged GCC. ROI1 in KE01 and ROI0 in KE02 and KE03 are at the landscape scale. ROI1 in KE01, ROI1 and ROI2 in KE02, ROI1, ROI2 and ROI3 in KE02 are at the vegetation community scale.

3.5. Vegetation cover records

Based on the field survey, the vegetation communities in Kapiti Farm can be categorized into four groups:

- Grass: only herbaceous vegetation;
- Acacia shrub: *Acacia drepanolobium* shrubs mixed with herbaceous layer;
- Diverse shrub: multiple shrub types mixed with herbaceous layer;
- Woodland: tall trees (>2m) and understory shrubs and herbaceous vegetation.

A total of 24 sample points, i.e., six samples for each vegetation community, were collected by Gachoki (2018) in October 2017 by using the global Land-potential Knowledge System (LandPKS) (Herrick et al., 2017). *Figure 1* shows the distribution of sample points. *Table A3* in Appendix shows the components of each vegetation community summarized from the information of all samples. These data were used to check if different vegetation communities had a distinct phenology.

3.6. Tools and platforms

Most image processing, data analysis and data visualization were implemented in Jupyter Notebook, which is a popular integrated development environment (IDE) for Python. *Table 2* shows all tools, platforms and important python packages used in this study.

Table 2: The list of tools, platforms and Python packages

Name	Version	Usage
Jupyter Notebook	5.5.0	Python IDE
PyCharm Community Edition	2018.1	Python IDE
QGIS	3.2.3	GIS data preview
ArcGIS	10.6.1	Shapefile editing
MATLAB	2018b	Statistical analysis
Google Earth Engine (GEE)		Image processing
Google Cloud Platform		Cloud computation
Google Drive		Cloud storage
Python 3.6.5 packages		
GDAL	2.2.2	Image processing
rasterio	0.36.0	Image processing
earthengine-api	0.1.146	Image processing
pandas	0.23.0	Data manipulation
NumPy	1.14.3	Data manipulation
pickle	4.0.0	Data serializing and de-serializing
netCDF4	1.4.1	Multi-dimension data serializing and de-serializing
xarray	0.10.9	Multi-dimension data serializing and de-serializing
matplotlib	2.2.2	Data visualization
seaborn	0.8.1	Data visualization
scikit-learn	0.20.0	Machine learning
SciPy	1.1.0	Statistical analysis and curve fitting
lmfit	0.9.11	non-linear optimization and curve fitting
Google drive APIs	3.0.0	File uploading and downloading

4. METHODS

Figure 4 provides an overview of the methods used in this thesis. The pre-processing and VI time series generation have been described in Chapter 3. The cloud and shadow detection for PS images were conducted by using Random Forest- and monthly threshold-based supervised classification. The observations flagged as clouds or shadows were removed from VI time series before using the double hyperbolic tangent function to fit curves. The mapping comparison of the phenological metrics focussed on four phenological metrics that were retrieved from the fitted curves, and included the start of season, end of season, maximum VI value, and integral VI from the start of season to the end of season.

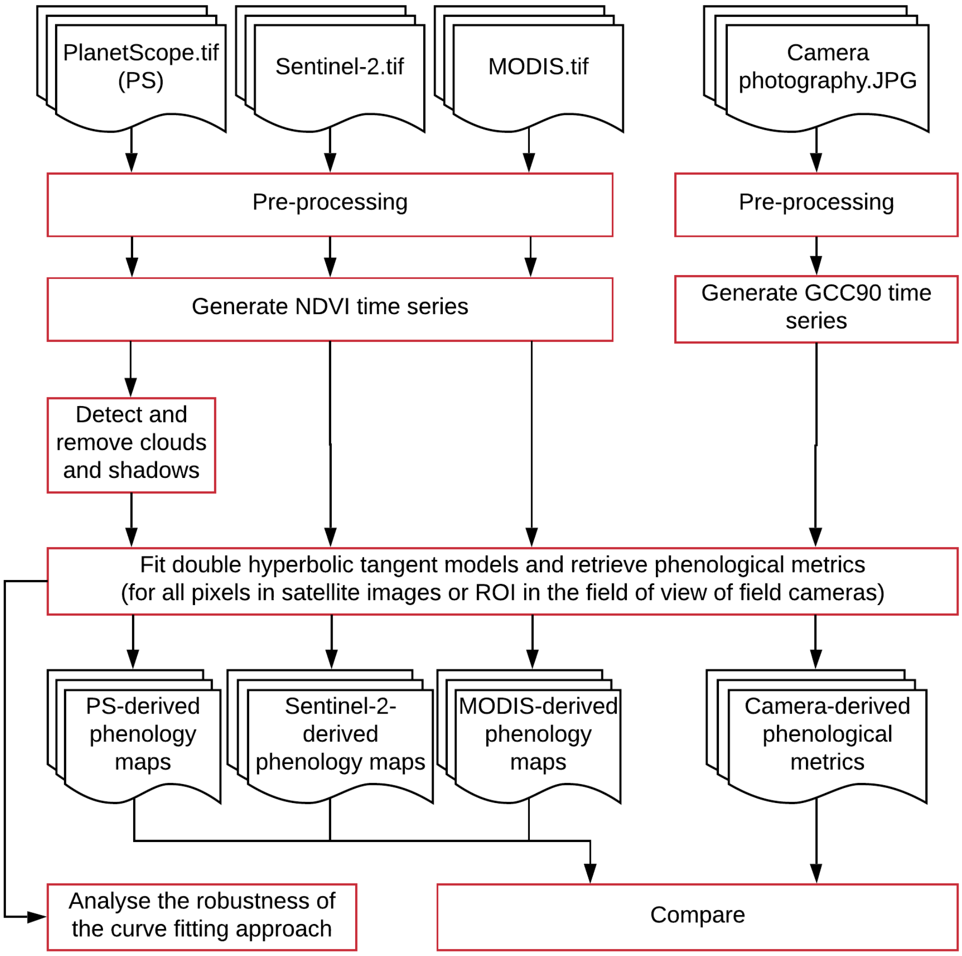

Figure 4: Overview of methods

4.1. Cloud and cloud shadow detection for PlanetScope images

Clouds and cloud shadows can block or contaminate the radiation reflected from the land surface to the sensor, which will cause abnormal values in VI time series used to retrieve phenological metrics (Champion, 2016; Tseng et al., 2008). Therefore the detection of clouds and cloud shadows is an essential step before analysing VI time series. However, there are no applicable cloud and cloud shadow masks or automated cloud and cloud shadow detection algorithms for PS images (Cooley et al., 2017). In most PS-based studies, clouds and shadows were manually digitized (Cooley et al., 2017), or only cloud-free images were used (Shi et al., 2018; Kääb et al., 2017).

In this study, clouds and cloud shadows were both classified based on thresholds of specific features (i.e., measurable properties of pixels in satellite images). The widely used features in existing cloud and cloud shadow detection algorithms, such as the cloud mask algorithm for MODIS (MOD35; Ackerman et al., 1997), the Automated Cloud Cover Assessment (ACCA) for Landsat-7 Enhanced Thematic Mapper (ETM) (Irish et al., 2006) and the Function of Mask algorithm (Fmask) (Zhu & Woodcock, 2012), are spectral features and temperature feature when thermal bands are available. The spectral features refer to the reflectance in spectral bands or the combination of reflectance in multiple spectral bands. The usually used spectral features include NIR, short-wavelength infrared (SWIR), the ratio of NIR to SWIR, NDVI, and the ratio of NIR to Green. Recently, spatial features quantified by grey level co-occurrence matrices (GLCM) were also found to be useful for cloud detection (Ghasemian & Akhoondzadeh, 2018; Bai et al., 2016). *Table A4* in Appendix lists all 124 potentially useful features for cloud and cloud shadow detection that were considered to be further investigated in the next step.

To assess which of the 124 features has the potential to assist in detecting clouds or cloud shadows for PS images, the relative importance value of each feature was derived using a Random Forest (RF) classifier. RF was selected because it can easily handle data with large dimensions and is not seriously impacted by the collinearity (Belgiu & Drăgut, 2016). The RF-based feature importance analysis has three steps: feature generation, sample data extraction, and RF training. To generate sample data to feed the RF classifier, 12 images captured in different months were manually digitized into three groups of polygons, i.e. cloud shadow, cloud, and clear. In other words, each pixel in these 12 images was given a label. To reduce spatial autocorrelation, only a limited number of pixels were randomly selected in the extent of each polygon. The number of samples was proportional to the area of each polygon. This resulted in a total of 2,963 shadow pixels, 2,949 cloud pixels and 5,979 clear pixels. These pixels that had one label and 124 features were fed to RF classifier to calculate the feature importance. The RF classifier was iterated for 100 times with the settings of 300 trees, one minimum samples leaf, and all features, as recommended by Belgiu & Drăgut, (2016). Each time 70% of training data were randomly selected, and the remainder 30% of data were used for validation. *Figure A1* in the Appendix shows the relative importance rank and relative importance value of each feature in each run. The feature importance is a relative value scaled from 0 to 1, and the higher values represent more contribution to discriminating clouds or cloud shadows. For cloud detection, the sum average of reflectance in Band 2 (b2_savg) and reflectance in Band 2 (b2) had relatively higher importance than other features. Regarding cloud shadow detection, the two most important features were the sum average of reflectance in Band 4 (b4_savg) and reflectance in Band 4 (b4). The GLCM-based "sum average" value of each pixel was calculated by dividing the sum of normalized grey tone values by the number of pixels within a 9x9 window (Bai et al., 2016). This texture feature that considers the reflectance value of surrounding pixels can identify contaminated pixels on the edge of thick clouds, which may be ignored when only based on spectral features.

The thresholds of b2, b2_savg, b4, and b4_savg were derived from cloud-free images by interpreting the image histograms. The values of cloud shadows are actually reduced reflectance of land surface, which can vary due to the change of land surface over time, so a choice was made to use monthly thresholds derived from cloud-free images in each month instead of one fixed scene-based threshold. To extract the monthly thresholds of b2, b4, b2_savg, and b4_savg, the histogram of each feature was generated for all cloud-free images per month (*Figure 5e-f*). Given the existence of noise in the cloud-free images, instead of using the maximum and minimum value, the 1st and 99.9th percentile in each histogram were set as the monthly thresholds of each feature for clear pixels. *Table A5* in the Appendix lists the exact values of each threshold.

The decision tree (*Figure 6*) for the classification of clear, clouds, and cloud shadows was generated by logically combining monthly thresholds of b2, b2_savg, b4 and b4_savg. *Figure 5a-d* shows that pixels labelled as cloud shadows in the sample image had lower values for b4 and b4_savg than clear pixels. In contrast, cloudy pixels had higher values for b2 and b2_savg. All 208 merged PS images were classified into three classes based on the decision tree. To further reduce the edge effect of clouds and cloud shadows, a buffer of three pixels was created around identified cloud and shadow pixels. A Python script (*https://gist.github.com/YanCheng-go/6f692136ab05e1f2345892fd0abb03dc*) was developed to automate the cloud and cloud shadow detection process for PS images.

Another group of manually labelled pixels, which also includes 2,963 shadow pixels, 2,949 cloud pixels and 5,979 clear pixels and differs from the sample data fed to RF classifier, were used as reference data to assess the accuracy of cloud and shadow detection at the pixel level. Despite the uncertainty of the process of labelling, the result can still reflect the relative accuracy of cloud and cloud shadow detection (Zhu & Woodcock, 2012). To evaluate if this algorithm is also effective for detecting clouds and shadows in other areas with different land covers as compared to Kapiti Farm, a number of PS images over an agricultural and a forest area in Aberdare National Park in Kenya were classified using monthly thresholds of b2, b2_savg, b4 and b4_savg derived from cloud-free images in the testing areas.

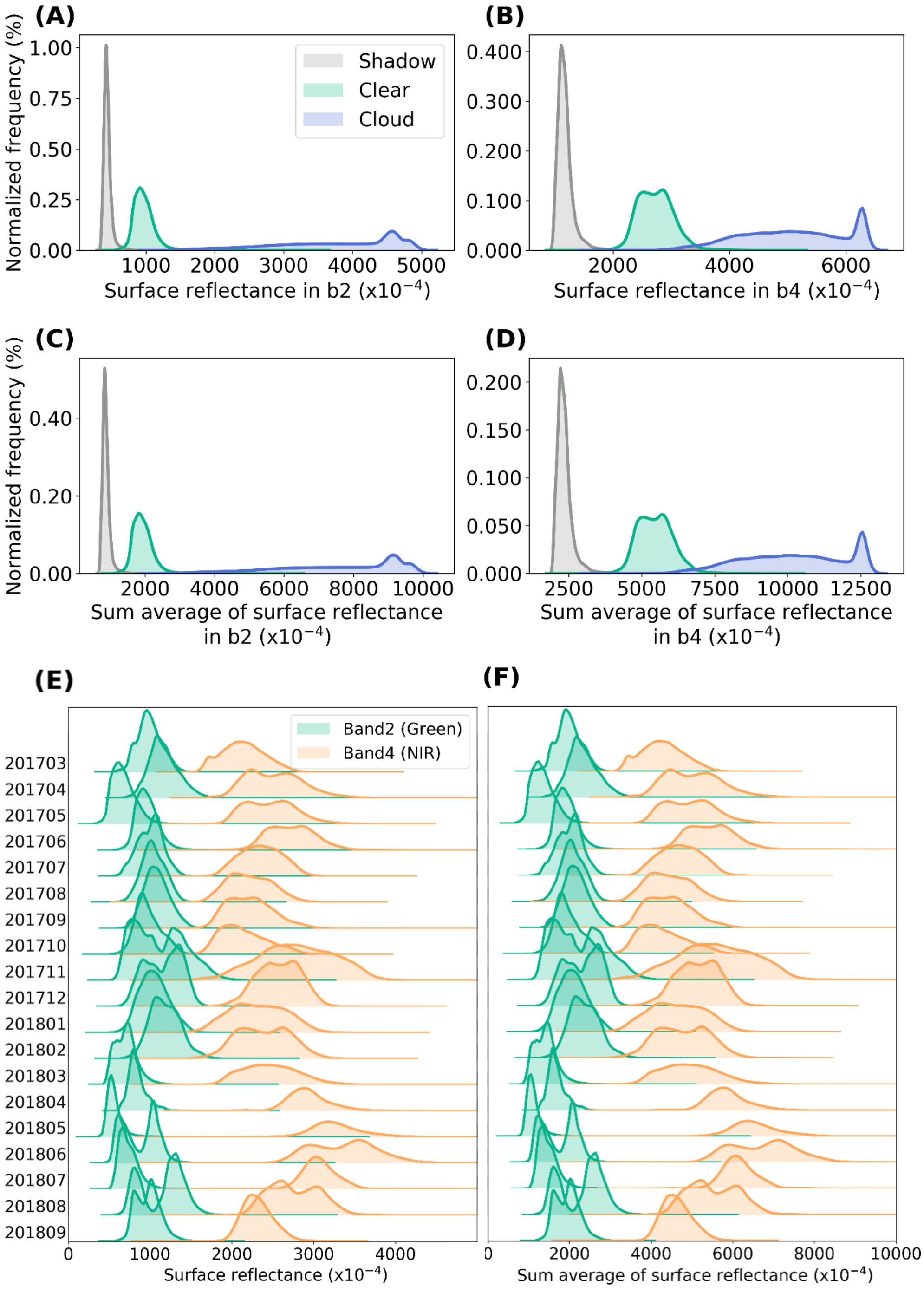

Figure 5: Histograms of surface reflectance and sum average surface reflectance in b2 and b4. (A) - (D) was extracted from a sample PS image captured in 24 June 2017. (E) and (F) shows the histograms of b2, b2_savg, 4, and b4_savg extracted from cloud-free PS images per month.

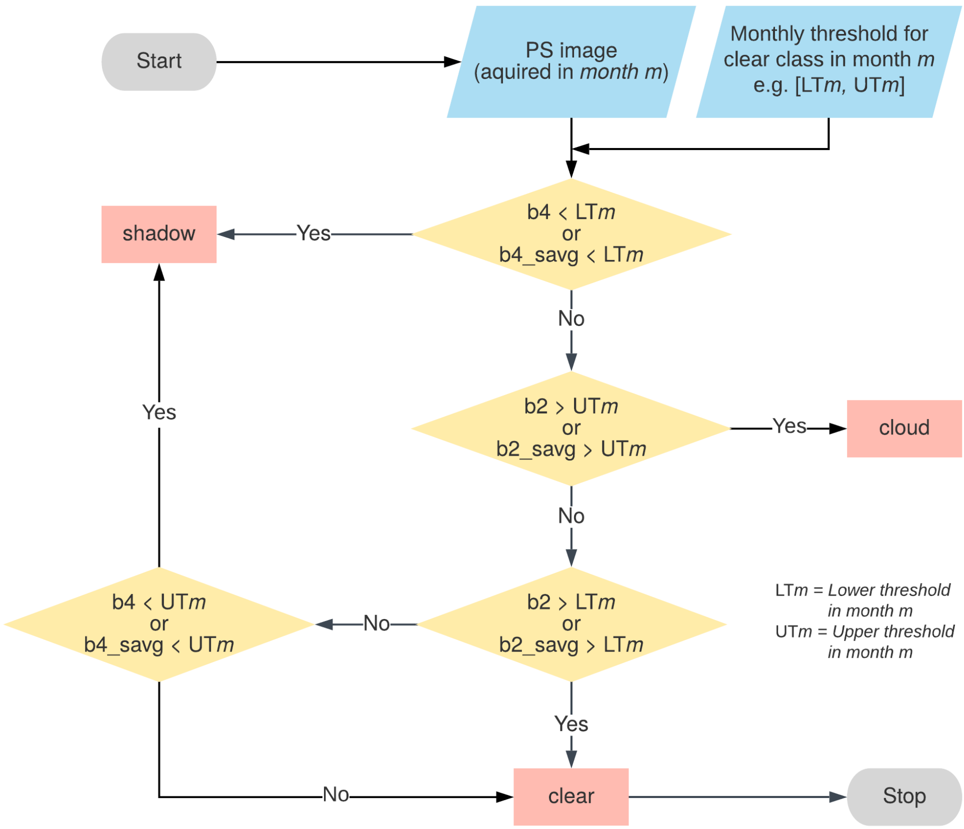

Figure 6: Decision tree using monthly thresholds of the surface reflectance in Band 2 (b2), the sum average of the surface reflectance in Band 2 (b2_savg), the surface reflectance in Band 4 (b4) and the sum average of the surface reflectance in Band 4 (b4_savg). The monthly thresholds for clear class for Kapiti Farm is shown in Table A5 in Appendix. UTm refers to the upper threshold in month m and LTm refers to the lower threshold in month m.

4.2. Double hyperbolic tangent function-based phenological metrics estimation

Many fitting models have been used to interpolate VI time series based on limited observations and resulting in a smooth VI time series. The most commonly-used models are Fourier transformation (Jakubauskas et al., 2001), asymmetric Gaussian function (Jonsson & Eklundh, 2002), Whittaker smoother (Eilers, 2003), and double-logistic algorithm (DL) (Beck et al., 2006). Atkinson et al. (2012) found phenological metrics estimated based on the four fitted models had less than one week difference, based on a study with Level 3 Medium Resolution Imaging Spectrometer images (spatial resolution ~4.6 km) across India.

In this study, an equivalent of DL, the double hyperbolic tangent function (Meroni et al., 2014) was used to fit models for VI time series generated from camera photos and satellite images, i.e., GCC90, $NDVI_P$, $NDVI_S$, and $NDVI_M$. The double hyperbolic tangent function can be written as:

$$VI(t) = a_0 + a_1 \frac{tanh[(t-a_2)*a_3]+1}{2} + a_4 \frac{tanh[(t-a_5)*a_6]+1}{2} - a_4 \quad (2)$$

where t refers to the day of year (DOY) and a_0, a_1, a_2, a_3, a_4, a_5, and a_6 are the user-specified function parameters, which are described as follows:

- a_0: the minimum VI value in the green-up phase;
- $a_1(a_4)$: the difference between the maximum and minimum VI value in the green-up (senescence) phase;
- $a_2(a_5)$: the time of midterm in the green-up (senescence) phase;
- $a_3(a_6)$: the constant used to adjust the slope at the midterm, initial value is equal to 0.02 (-0.02).

A Python script (*https://gist.github.com/YanCheng-go/d4e17831f294199443d0f7682558e608*) (*Figure A9 in Appendix*) was developed to execute the curve fitting for each VI series. In the script, the Levenberg-Marquardt algorithm (More, 1978) in lmfit Python package (Newville et al., 2014) was used to find the optimum model parameters that minimize the sum of squared residuals between fitted values and actual values. Lower VI values can be a result of remaining contamination of atmospheric effects and unclassified clouds and shadows, so the fitted curves were adapted to the upper envelope based on an iterative weighing method used by Meroni et al. (2014) and Vrieling et al. (2018). In short, if the observations (y_i) in original VI time series are smaller than the corresponding fitted values ($f(x_i)$), the weights of those observations in next curve fitting will be decreased (Eq. 3). As a consequence, the next fitted curve will be closer to observations with higher VI values. The initial weights of all observations were set as 1. The iteration stops when the n^{th} sum of weighted absolute residuals (SWAR) (Eq. 4) is smaller than $(n+1)^{th}$ SWAR or the iteration times equal to a customized maximum threshold. The preliminary tests indicated that for PS-based NDVI time series in more than 90% of the case less than five iterations were used before the fitting converged. To avoid infinite iterations, the maximum iteration time was set as 10. It is worth noting that, if the number of observations is less than the number of parameters of the user-defined function (double hyperbolic tangent function), the curve fitting algorithm will not work.

$$Weight_i = 1 - \frac{|y_i - f(x_i)|}{max(|y - f(x)|)}, when\ y_i - f(x_i) \le 0 \quad (3)$$

$$SWAR = \sum_{i=1}^{n} Weight_i * |y_i - f(x_i)| \quad (4)$$

As introduced in Chapter 3, the timeframe of this study was from 1 March 2017 to 1 October 2018, which covers three vegetation seasons. To fit curves for each season separately, the timeframe was split into three parts: 1 March 2017 – 1 October 2017 (LR2017), 1 September 2017 – 1 March 2018 (SR2017), 1 February 2018 – 1 October 2018 (LR2018). To make sure that dry periods were included, there were one-month overlapping periods between successive vegetation seasons. As shown in *Figure 2*, the first rainy season in

2017 started in April and was one month later than in 2018, so the timeframe for LR2017 set in the study was one month later than for LR2018. For field camera series, the curve fitting was applied for both landscape-level ROI and species-level ROIs in the field of view of three cameras (*Figure 3*). For satellite images, the curve fitting was applied for all individual image pixels contained in Kapiti Farm.

After fitting curves for satellite- and camera-derived VI time series (i.e., GCC90 and NDVI), two temporal metrics, the date of the start of season (SOS) and the date of the end of season (EOS), were estimated from the fitted curves. This estimation can be based on four types of thresholds: absolute VI, proportions of maximum VI, proportions of amplitude, and slopes of VI curves (Misra et al., 2018). Most phenology-related studies extract the date (SOS or EOS) when VI values reach a specific proportion of amplitude in VI time series. The 50% threshold of amplitude, which indicates the time of fastest green-up or senescence (Vrieling et al., 2017; White et al., 1997), was used in this study. Apart from SOS and EOS, two NDVI-related phenological metrics were retrieved from satellite-derived NDVI time series. maxNDVI relates to maximum biomass levels and species richness, whereas cumNDVI is often used as a proxy for seasonal productivity (Heumann et al., 2007; Bailey et al., 2004). This results in the following four metrics:

- SOS_{50}: the start of the season; the DOY when VI first reaches 50% of the difference between the maximum and minimum VI in green-up phase;
- EOS_{50}: the end of the season; the DOY when VI first reaches 50% of the difference between the maximum and minimum VI in the senescence phase;
- maxNDVI: the maximum NDVI;
- $cumNDVI_{50}$: the accumulation of NDVI between SOS_{50} and EOS_{50}.

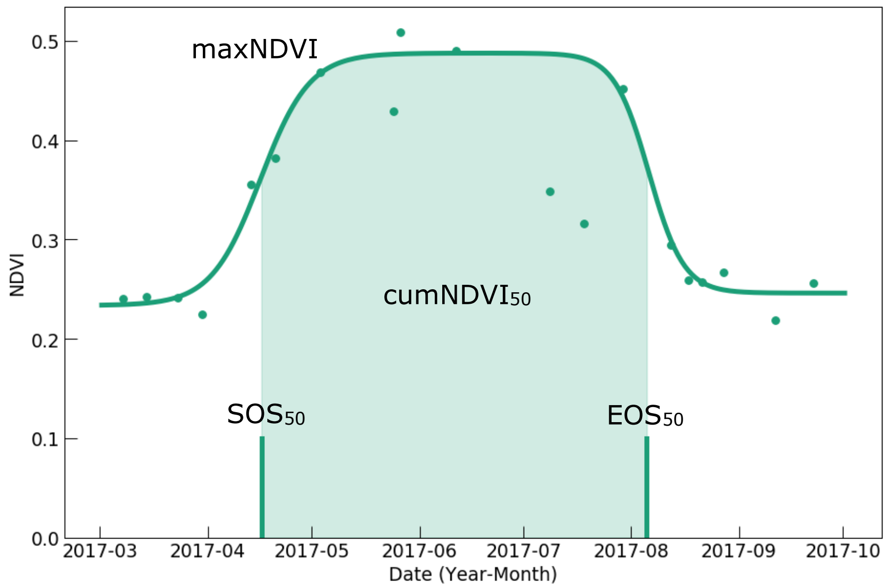

Figure 7: Illustration of four phenological metrics retrieved from a fitted curve.

4.3. Statistical analysis and comparison of phenology metrics

Based on the phenological metrics estimated from PS-, Sentinel-2- and MODIS-derived NDVI time series and camera-derived GCC90 time series, a number of analyses were executed to 1) link satellite-derived phenological metrics to camera-derived ones; 2) compare PS-derived phenological metrics to Sentinel-2- and MODIS-derived ones; 3) investigate the impact of image availability on PS-based estimates of phenological metrics. Different statistical measures were used for these analyses, including: 1) Root Mean Squared Deviation (RMSD) for quantifying the difference across datasets, 2) Mean Signed Deviation (MSD) for assessing the bias, and 3) R^2 or Pearson's correlation coefficient (r) for evaluating the correlation between two datasets.

To assess the performance of curve fitting, r, RMSD, and MSD were calculated for each fitted VI time series as compared to the original VI time series. The low values of r, RMSD or MSD do not necessarily mean a bad performance of curve fitting because of the implementation of upper envelope fitting. Nevertheless, the comparison of r, RMSD and MSD can indicate the relative goodness of curve fitting across data sources (Vrieling et al., 2017).

For the comparison of satellite- with camera-derived phenological metrics, to match the field of view of cameras as well as mitigating geometric errors, PS images were first aggregated to 10 m resolution by taking the average of pixel values, only if the centre of the pixel falls in 10x10 m cells. The SOS_{50} and EOS_{50} retrieved from the aggregated PS, Sentinel-2 and MODIS NDVI time series for the pixels corresponding to three camera locations were then compared against the SOS_{50} and EOS_{50} from the camera-derived GCC90 time series. The GCC90 time series used in this analysis were extracted only for the landscape-level ROI in the field of view of each camera. The RMSD and MSD between satellite-derived and camera-derived phenological metric were used to quantify the difference.

To compare PS-derived phenological metrics to metrics derived from Sentinel-2 and MODIS, PS-derived phenology maps were resampled to 10 m and 250 m resolution by taking the average of pixel values, only if the centre of the pixel falls in 10x10 m and 250x250 m cells. After that, density scatterplots were generated and the R^2, RMSD, and MSD were calculated to evaluate the relationship between phenological metrics derived from different satellite images.

To assess the impact of reduced image availability on the estimation of phenological metrics with PS, two simulation analyses were executed. The first one mimics the reduced availability by randomly removing n% (with n varying from 5 to 50) of observations from the original NDVI time series. The 27 NDVI time series used in this analysis corresponded to the 24 vegetation samples and the three camera locations. A total of 100 iterations of randomly removing observations was done for each n and NDVI time series. The four phenological metrics were then retrieved from each fitted curve. For each n and location, the RMSD for SOS_{50} and EOS_{50} and the RMSD against the value derived from full dataset (RRMSD) for maxNDVI and $cumNDVI_{50}$ were then calculated through comparing the 100 retrieved values against the value retrieved from the original NDVI time series as the base. This resulted in 27 (R)RMSD values for each phenological metric per season. The mean and standard deviation of those 27 (R)RMSD values were also calculated. The (R)RMSD were used to reflect the potential "error" of phenological metrics retrieved based on a reduced number of observations in the NDVI time series. This analysis can also indicate which metric is more sensitive to the lack of observations.

The second simulation analysis examined in which period of the season reduced data availability would most significantly affect phenology estimation. To achieve this, all observations in every first or second half of a month, i.e. 1-15March, 16-31March, were iteratively removed from the NDVI time series. Remaining observations were used to fit curves and retrieve phenological metrics. This process was also implemented for 24 vegetation samples and three camera locations (*Figure 1*). (R)RMSD and MSD were used to illustrate the deviation between phenological metrics retrieved from original NDVI time series and the modified NDVI time series for which ~15 days of observations were removed.

5. RESULTS

5.1. Cloud and cloud shadow detection for PlanetScope images

The monthly threshold-based cloud and shadow detection algorithm (Section 4.1) was implemented on 208 merged PS images. Visual inspection of classification results revealed a reasonable cloud/cloud shadow detection for most images. *Table 3* summarizes the classification accuracy based on the manually labelled reference data. *Figure 8* shows examples of classified images and highlights incorrect classification areas. It suggests that the designed cloud and cloud shadow detection algorithm tended to underestimate clouds and cloud shadows, i.e. the omission error for clouds and cloud shadows is 33% and 26.05%, respectively. The underestimation of clouds was mostly caused by semi-transparent clouds, such as cirrus and thin clouds on the edge of thick clouds (*Figure 8a, c and d*). The reason for the underestimation of cloud shadows (*Figure 8a*) may be that the spectral response of cloud shadows is at times similar to clear vegetated areas. Despite the underestimation of clouds and cloud shadows, the implementation of upper envelope curve fitting can further mitigate the influence of those undetected clouds and cloud shadows that have lower NDVI values in time series. However, when there are only a small number of observations in NDVI time series, the contaminated observations can still result in biased curve fitting.

Figure 9 shows the average number of valid observations per pixel per month. When comparing to *Figure 2*, it is clear that in drier months the number of valid observations was larger than during wet months. The statistical analysis also revealed that there was a strong correlation ($r = 0.62$, $p = 0.004$) between the average number of cloud-free observations per month and monthly precipitation.

To test if the designed cloud and cloud shadow detection algorithm is effective in areas with other land cover types, an agricultural and a forest area outside the Kapiti Farm in Kenya were also classified by the same algorithm. Specifically, a number of images within the boundary of testing areas were classified using monthly thresholds of b2, b2_savg, b4, and b4_savg derived from cloud-free images in the testing areas. The classified images are shown in *Figure 10*. Overall, the designed algorithm seems to be effective for various land covers, including agriculture and dense forest areas that are not found in Kapiti Farm.

Table 3: Confusion matrix of image classification

Classified / **Reference**	**Cloud shadow**	**Cloud**	**Clear**	**Total**	**Omission error (%)**	**Producer accuracy (%)**
Cloud shadow	2191	0	772	2963	26.05	73.95
Cloud	40	1976	933	2949	33.00	67.00
Clear	50	153	5776	5979	3.40	96.60
Commission error (%)	3.95	7.19	22.8			
User accuracy (%)	96.05	92.81	77.20			

Overall accuracy: 83.62%

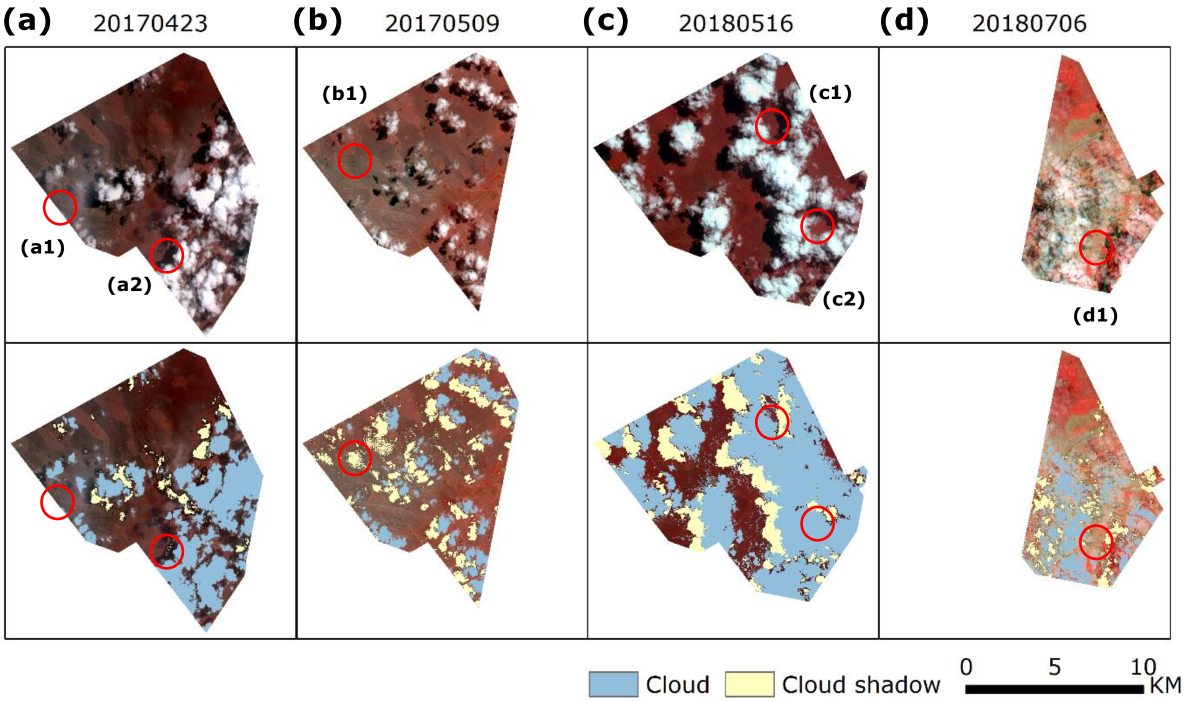

Figure 8: Examples of classified images. The first row shows false colour composite images (NIR, red and green bands). The second row shows classified images. The red circles highlight locations for which the classification did not produce accurate results. (a1) undetected haze area. (a2) undetected shadow area. (b1) shadow detection in clear area. (c1) cloud detection in clear areas. (d1) undetected cirrus.

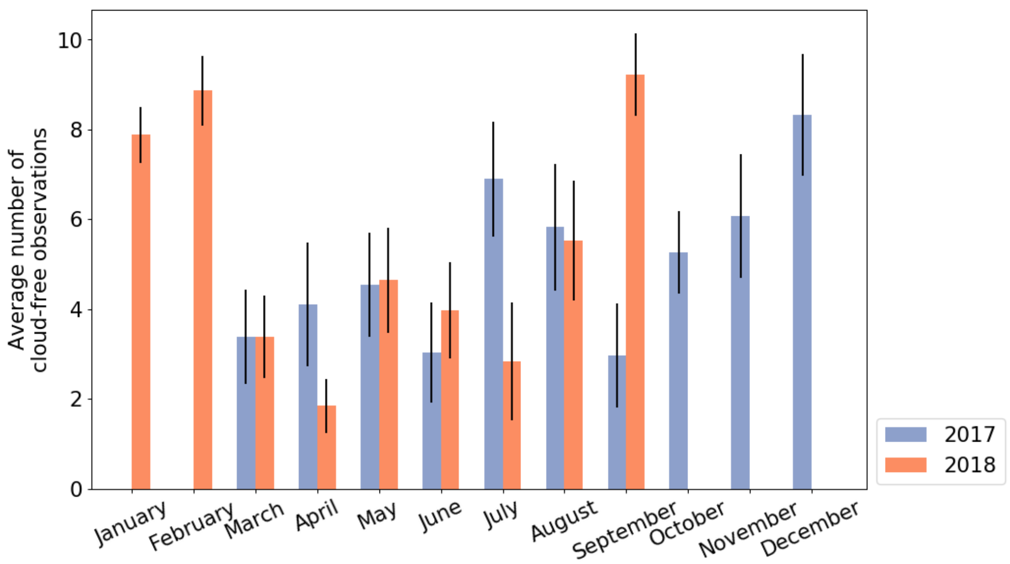

Figure 9: Average number of cloud-free observations per pixel and per month. The vertical line on the top of each bar indicates the standard deviation.

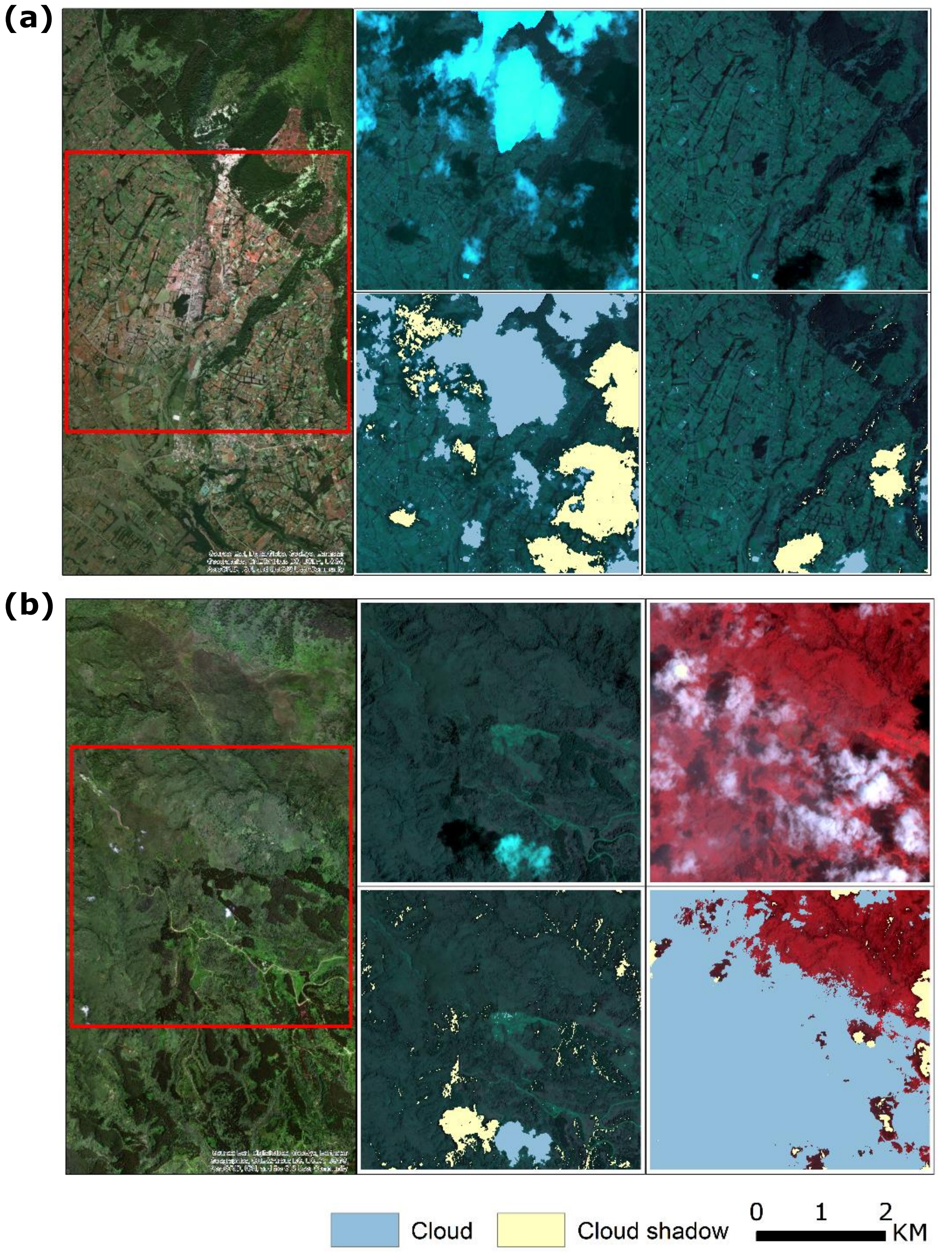

Figure 10: Examples of classified images in (a) agricultural and (b) forest areas in Aberdare National Park in Kenya. The second and third columns show false colour composite images (NIR, red and green bands).

5.2. Satellite- versus camera-derived phenological metrics

Figure 11 compares the GCC90 time series of different vegetation types in the field of view of KE01, KE02 and KE03. As illustrated in *Table A3* in Appendix and *Figure 3*, the dominant vegetation communities at these three locations are open grass, mixed grass/shrubs (*Acacia drepanolobium*) and grass/trees (acacia species), respectively. The phenological metrics estimated from GCC90 time series were different across vegetation communities. The EOS_{50} of shrubs and trees in two seasons are both later than for grass. The time lag was varying along with the increase of precipitation from SR2017 (281.5 mm) to LR2018 (656.5 mm). On average, after the grass entered senescence phase, the shrubs and trees maintained the leaf canopy for about one more month. The SOS_{50} of grass was later than that of shrubs while earlier than trees in both seasons. Overall, grass has shorter growing seasons and is more sensitive to precipitation variations than shrubs and trees. This difference was also found in a prior camera-based phenology study for semi-arid lands (Liu et al., 2017). It is worth noting that the trees and grass in the field of view of KE03 had a short secondary green-up phase after the main green-up phase in SR2017 and LR2018 (*Figure 11c*), which was respectively caused by a dry period in December 2017 followed with substantial rainfall in January 2018 and a light rainfall in 31 July 2018 (*Figure 11d*). However, the open grass in the field of view of KE01 and the mixed grass /shrubs in the field of view of KE02 have no apparent secondary green-up phases. Moreover, the speed of green-up for the grass/understory grass in the field of view of KE03 is faster than the grass in the field of view of KE01 and KE02. This can be explained by that the trees in KE03 may contribute to reducing the evaporation in the understory vegetation (Akpo, 1997). In short, the camera-based analysis indicates that vegetation phenology in Kapiti Farm is spatially and temporally heterogeneous, for which the complex composition of vegetation and rainfall variability may be the main factors.

Figure 12 compares satellite-derived NDVI time series with camera-derived GCC90 time series for the three camera locations. The camera-derived GCC90 time series were calculated for the entire field of view to simulate the landscape scale as in satellite images. Because of the larger amount of precipitation during LR2018 as compared to SR2017, the maximum satellite NDVI values were larger in LR2018. However, for KE01 the maximum GCC90 is smaller for LR2018, which may be explained by experienced problems with overexposure during that season. Despite these problems, a clear seasonal signal is still visible. The PS-derived NDVI time series show noisier temporal patterns as compared to Sentinel-2 and MODIS-derived NDVI. Reasons for this difference could be: 1) the cloud and cloud shadow screening for PS images is not of the same quality as for Sentinel-2 and MODIS images, partially due to missing dedicated spectral bands for, e.g., cirrus detection; 2) the PS images were captured at different local solar time; 3) the quality of PS surface reflectance products is not as good as Sentinel-2 and MODIS. Nevertheless, the denser NDVI time series derived from PS images could be potentially better in capturing vegetation variations in short terms than other two sparse NDVI time series derived from MODIS and Sentinel-2 images. *Table 4* compares satellite- with camera-derived SOS_{50} and EOS_{50}. On average, the difference (RMSD) between satellite- and camera-derived SOS_{50} was ~6 to ~9 days. MODIS-based SOS_{50} retrievals were more similar to those from the camera series, as compared to PS and Sentinel-2. Moreover, PS- and Sentinel-2-based SOS_{50} retrievals were usually later than those from the camera series. MODIS-based SOS_{50} retrievals were earlier than camera-derived in SR2017 ones while later than camera-derived ones for LR2018. The RMSD for EOS_{50} is approximately twice as large as for SOS_{50}. PS-based EOS_{50} retrievals were closer to those from the camera series, as compared to MODIS and Sentinel-2.

Table 4: Comparison of satellite-derived SOS_{50} and EOS_{50} with camera-derived ones.

	SOS50			EOS50		
	PS	**Sentinel-2**	**MODIS**	**PS**	**Sentinel-2**	**MODIS**
RMSD	9.56	9.44	6.38	17.26	19.82	21.64
MSD	6.33	6.17	0.67	7.00	5.00	12.50

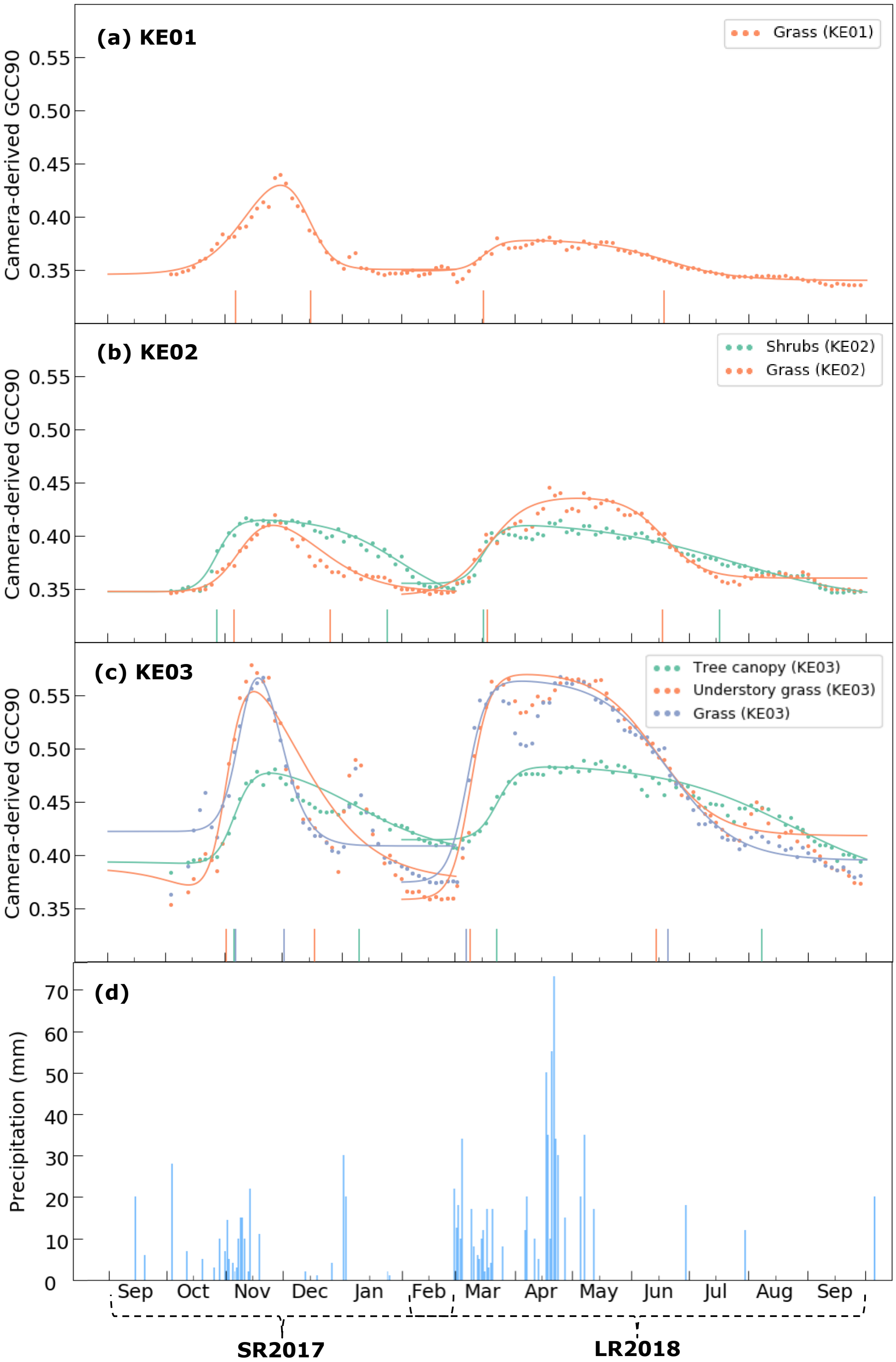

Figure 11: Time series of GCC90 for each vegetation community in the field of view of KE01, KE02 and KE03. In panel a-c, the lines are fitted curves and the vertical lines near x-axis indicate the SOS_{50} and EOS_{50} retrieved from each fitted curve. Panel d shows the daily precipitation in SR2017 and LR2018. The four plots use the same x-axis.

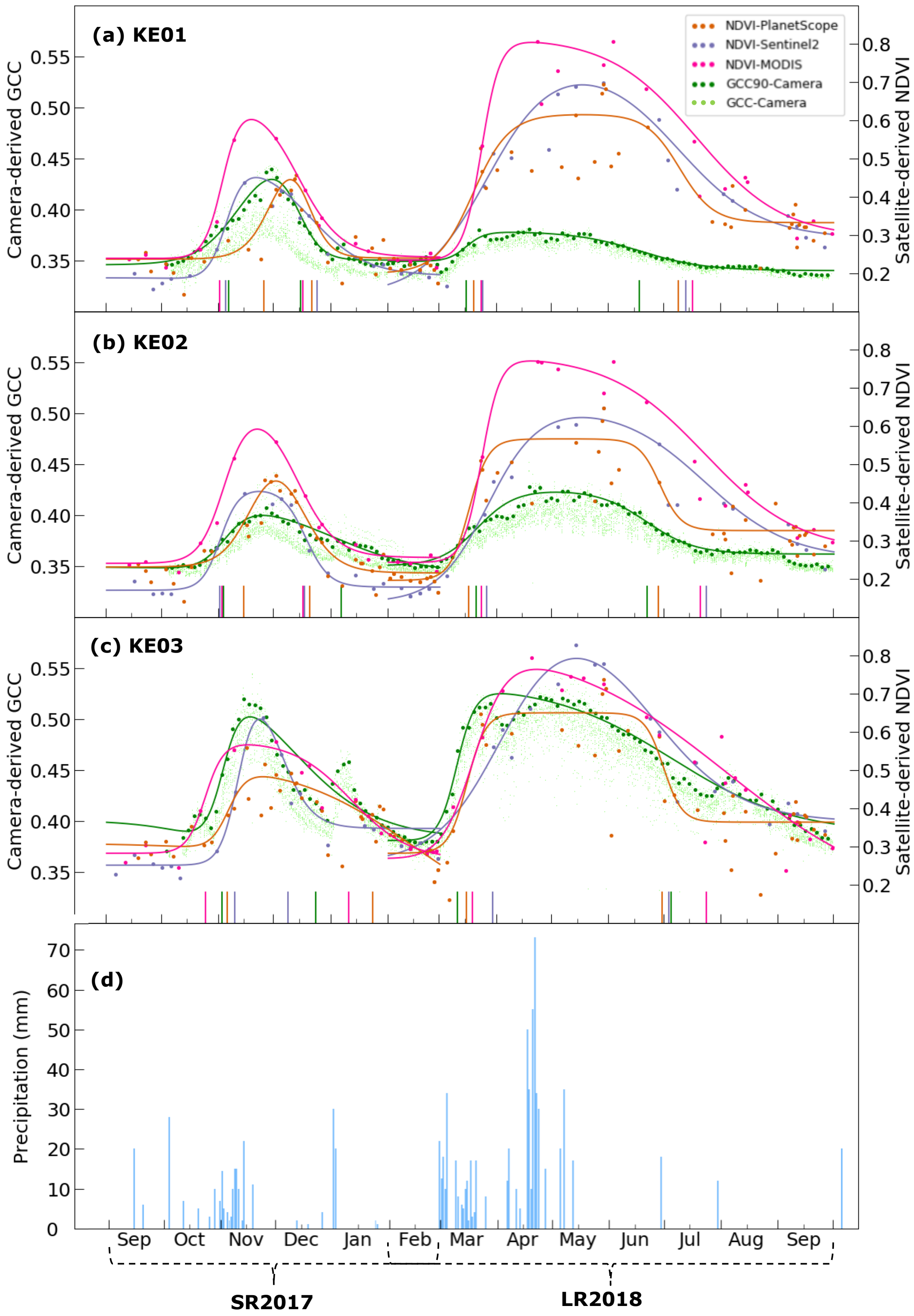

Figure 12: Time series of satellite-derived NDVI and camera-derived GCC90 at three camera locations (KE01, KE02, and KE03) in SR2017 and LR2018. GCC90 were extracted for the entire field of view at each camera locations.

5.3. PlanetScope-derived phenology maps

The curve fitting process was implemented for PS-derived NDVI time series for each pixel within Kapiti Farm boundary. *Figure 13* shows the maps of SOS_{50}, EOS_{50}, maxNDVI and $cumNDVI_{50}$ for the three seasons considered. Various maps clearly show a spatial resemblance to differences in land surface (*Figure 1*), although the spatial patterns of each metric are different across three seasons. It is worth noting that, there is an apparent artefact in *Figure 13f*, i.e. a clear north-south linear pattern can be discerned with later EOS_{50} dates west of the imaginary line. Further examination revealed that this was caused by the 17 July 2017 image, which only covered the north-western part. As shown in *Figure 14*, after removing the observation on 17 July 2017 from the time series of the west of the imaginary line, the difference of EOS_{50} decreased from ~10 to ~2 days. This suggests that, even though there are many valid observations in PS-derived NDVI time series, a single observation can have an important influence on the curve fitting and phenological metrics estimation.

The mean and standard deviation of each phenological metric are shown in *Figure 13*. The average time of the first start of season in 2018 (81 ± 4.66) is more than one month earlier than in 2017 (121 ± 7.49). This can be explained by the variation of precipitation. As shown in *Figure 2*, the first rains of the LR season in 2017 were approximately one month later than in 2018. In addition, the amount of precipitation in LR2018 was greater than in LR2017, as a consequence of which the date of the first end of season in 2018 (191 ± 11.47) is later than in 2017 (182 ± 10.73). The relatively high maxNDVI and $cumNDVI_{50}$ in LR2018 as compared to other two seasons is also a result of the large amount of precipitation in March and April in 2018 (*Figure 2*).

Table 5 summarizes the four phenological metrics for the 24 sample points that were categorized into four vegetation groups. The composition of each vegetation group is shown in *Table A3* in the Appendix. The one-way ANOVA analysis indicates that the four phenological metrics are not significantly (significance level = 0.1) different between the vegetation communities. The reason could be that: 1) each vegetation group only contains a small number of samples; and 2) multiple vegetation types exist within a group, whereby mostly grass is the dominant signal. But the comparison of the average values of each metrics can still provide some information. For example, except the $cumNDVI_{50}$ for LR2017, the maxNDVI and $cumNDVI_{50}$ for the group of mixed acacia trees and grass (group D) is slightly higher than other groups.

Table 5: Phenological metrics retrieved from PS-derived NDVI time series for sample points and per rain season. SOS_{50} and EOS_{50} are expressed as Day of the Year (DOY). Group A, B, C and D refer to four vegetation communities. A = Diverse shrubs, B = Acacia trees with grass, C = Open grassland, D = acacia shrubs with understory grass. Each vegetation group contains six sample points. The phenological metrics are reported as the average of six observations.

	LR2017				**SR2017**				**LR2018**			
	A	**B**	**C**	**D**	**A**	**B**	**C**	**D**	**A**	**B**	**C**	**D**
SOS_{50}	120	119	118	118	317	320	319	320	80	80	82	80
EOS_{50}	188	176	183	187	362	374	357	365	189	188	193	193
maxNDVI	0.50	0.56	0.48	0.49	0.47	0.52	0.47	0.47	0.65	0.69	0.67	0.65
$cumNDVI_{50}$	32.2	29.2	28.1	30.4	19.3	25.8	16.0	19.1	68.0	71.2	67.6	69.2

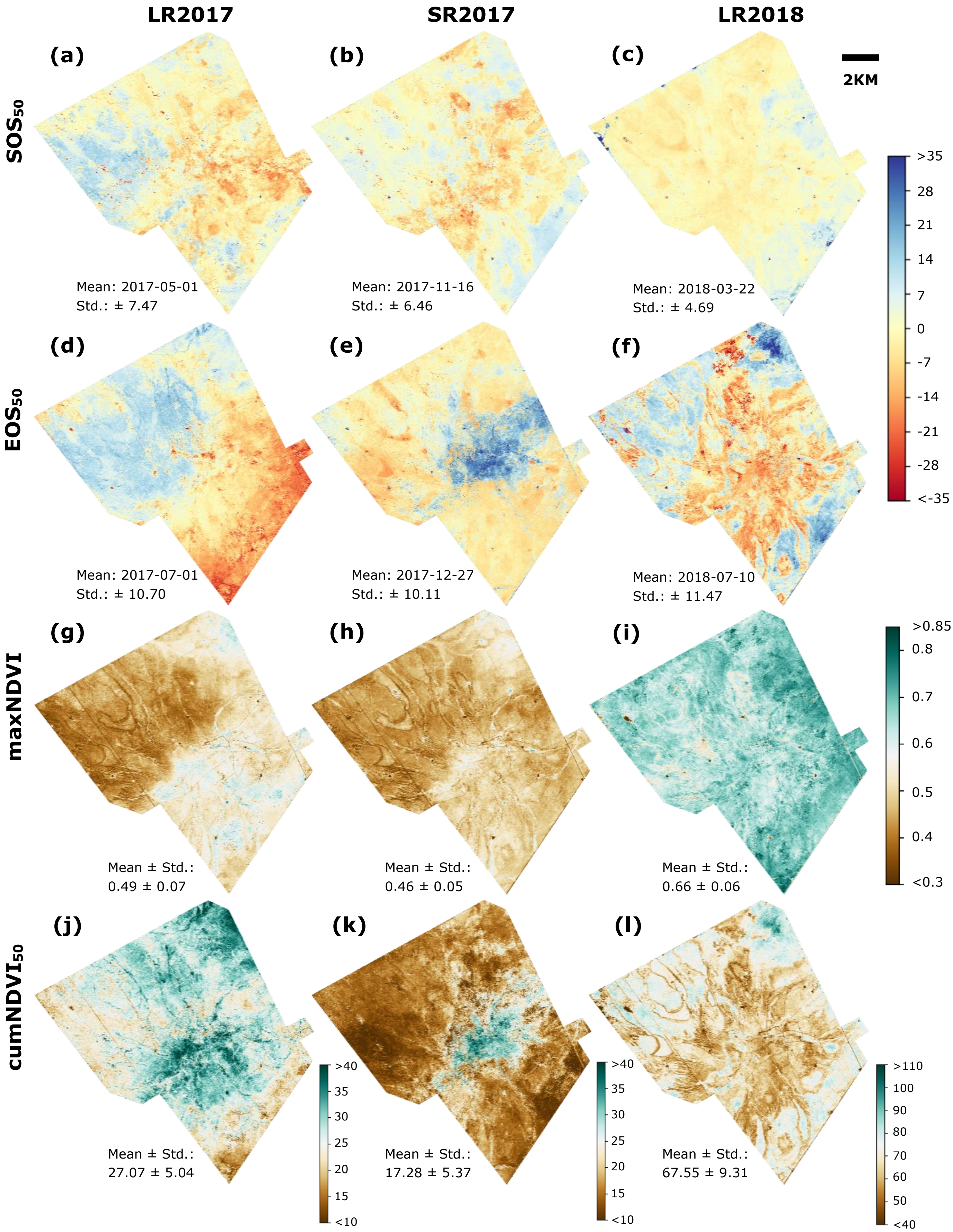

Figure 13: Phenology maps derived from PS images. The mean and standard deviation are reported for each map. SOS_{50} and EOS_{50} maps are visualized by showing the difference (in days) from the spatial mean for each season. Red colours indicate that the date is before the mean, and blue colours indicate that the date is after the mean.

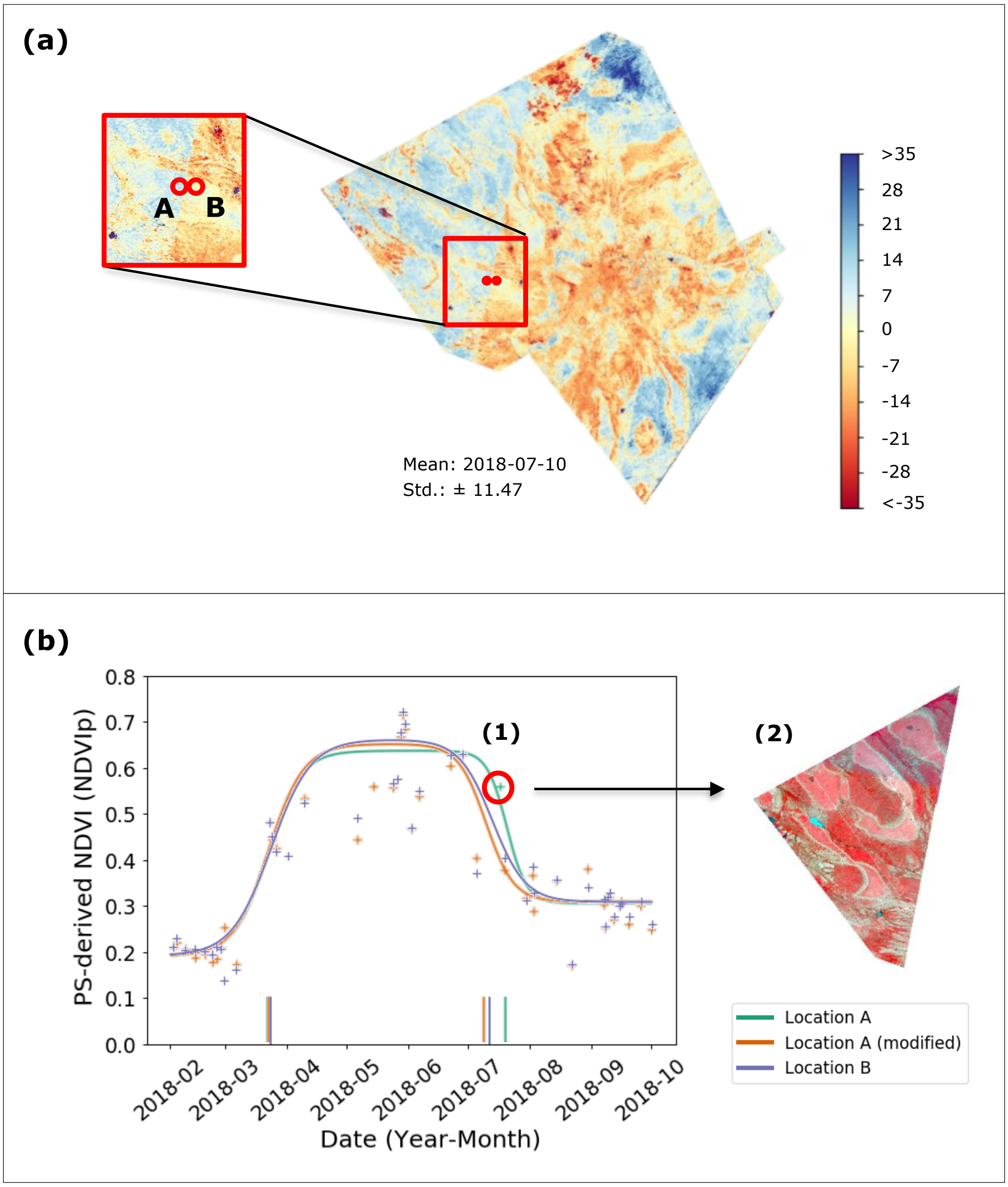

Figure 14: Illustration of the linear artefact in PS-derived EOS$_{50}$ map (Figure 13f). Panel a is the enlarged map that is zoomed in to the artefact. The EOS$_{50}$ map is visualized by showing the difference (in days) from the spatial mean for each season. Red colours indicate that the date is before the mean, and blue colours indicate that the date is after the mean. In panel b, the green and blue lines are fitted curves for pixel A and B, which are highlighted in frame a. The red curve is the fitted curve after removing the observation on 17 July 2018. SOS$_{50}$ and EOS$_{50}$ derived from each fitted curve are indicated as vertical lines near x-axis. Images (2) in panel b is the PlanetScope image acquired on 17 July 2018 and displays by false colour composite (red, NIR and blue bands).

5.4. PlanetScope- versus Sentinel-2- and MODIS-derived phenological metrics

Table 6 compares the image availability and the fit statistics of PS, Sentinel-2 and MODIS. The average number of cloud-free observations for PS images in SR2017 and LR2018 are almost twice as many as the number of cloud-free observations for Sentinel-2 and MODIS images. The maximum gap (in days) between two sequential observations is also smaller for PS as compared to than Sentinel-2- and MODIS for LR2017 and SR2018. However, for LR2018, this difference was negligible due to the very persistent cloud cover in May 2018. More valid observations and shorter temporal gaps facilitate the ability to reveal larger temporal NDVI variations, which may not be due to noise only but also due to real within-season variability. Both a stronger noise and capturing of more natural variation may cause the smaller r value for PS. For example, in SR2017, there was a short secondary green-up after the main growing season (*Figure 12c*) caused by a dry period in December 2017 followed by substantial rainfall in January 2018. The double hyperbolic tangent function-based curve fitting can only model one peak per season, as a consequence of which the PS-derived r value in SR2017 was lower than in LR2018. For Sentinel-2, this second peak was not apparent, resulting in similar r values for SR2017 and LR2018.

Figure A4-A7 in Appendix compare the spatial pattern of each phenological metric derived from PS, MODIS and Sentinel-2. Overall, the phenology maps derived from three satellite images have similar spatial patterns. However, Sentinel-2 derived SOS_{50} map in LR2018 (*Figure A4h* in Appendix) shows apparent artefacts. The reason for these artefacts could be the lack of observations from March until the beginning of April in 2018 as illustrated in *Figure 15*, while a single image in that time-frame contains clouds, but for the non-cloudy areas strongly influences the fitting. Although MODIS-derived phenology maps do not have apparent artefacts, they show fewer details than PS- and Sentinel-2-derived phenology maps due to the coarse spatial resolution.

Figure 16 compares phenological metrics from Sentinel-2 and MODIS to phenological metrics from PS at the pixel level. The PS-derived phenological metrics were aggregated by taking the average of values within 10x10m and 250x250m cells for Sentinel-2 and MODIS, respectively. The maxNDVI and $cumNDVI_{50}$ shows a stronger correlation than SOS_{50} and EOS_{50}. The negative MSD of SOS_{50} means that on average SOS_{50} derived from Sentinel-2 and MODIS is later than SOS_{50} derived from PS. The MSD for Sentinel-2-derived SOS_{50} in LR2018 is an exception, which could be caused by the large area of artefacts in the Sentinel-2 SOS_{50} map (*Figure 15a*). The MSD values for EOS50 in SR2017 are negative while positive in LR2017. This difference could be caused by the apparent secondary green-up in SR2017. The RMSD values reported in *Figure 16* for SOS_{50} and EOS_{50} indicate that on average Sentinel-2-derived SOS_{50} and EOS_{50} had ~9 and ~12 days difference from PS-derived ones. For MODIS, the difference is similar to Sentinel-2. The negative MSD of SOS_{50} means that on average SOS_{50} derived from Sentinel-2 and MODIS is earlier as compared to PS. This finding matches the analysis by Vrieling et al. (2017) and Zhang et al. (2017).

Table 6: Comparison of image availability and fit statistics among PS, Sentinel-2 and MODIS. r, MSD and RMSD calculated from fitted and original NDVI values measure the goodness of fit. nImages refers to the average number of cloud-free observations in NDVI time series. maxGap indicates the maximum difference (days) between two continuous cloud-free observations in NDVI time series. Mean and standard deviation are reported for each measurement.

	LR2017		SR2017			LR2018		
	PS	**MODIS**	**PS**	**Sentinel-2**	**MODIS**	**PS**	**Sentinel-2**	**MODIS**
r	0.85±0.08	0.95±0.05	0.86±0.07	0.95±0.03	0.96±0.04	0.93±0.03	0.96±0.04	0.96±0.03
RMSD	0.054±0.02	0.03±0.02	0.046±0.01	0.55±0.19	0.031±0.01	0.034±0.01	0.03±0.01	0.05±0.02
MSD	-0.003±0.0	-0.012±0.0	-0.002±0.0	0.015±0.0	-0.012±0.0	-0.004±0.0	0.007±0.0	-0.017±0.0
nImages	29.69±2.49	18.09±1.61	39.37±2.78	20.93±2.20	17.24±1.58	41.02±3.28	22.17±2.48	20.93±2.03
maxGap	25.64±5.78	30.67±4.77	14.00±4.97	21.48±6.25	20.50±2.87	32.32±7.86	34.14±8.45	30.37±6.11

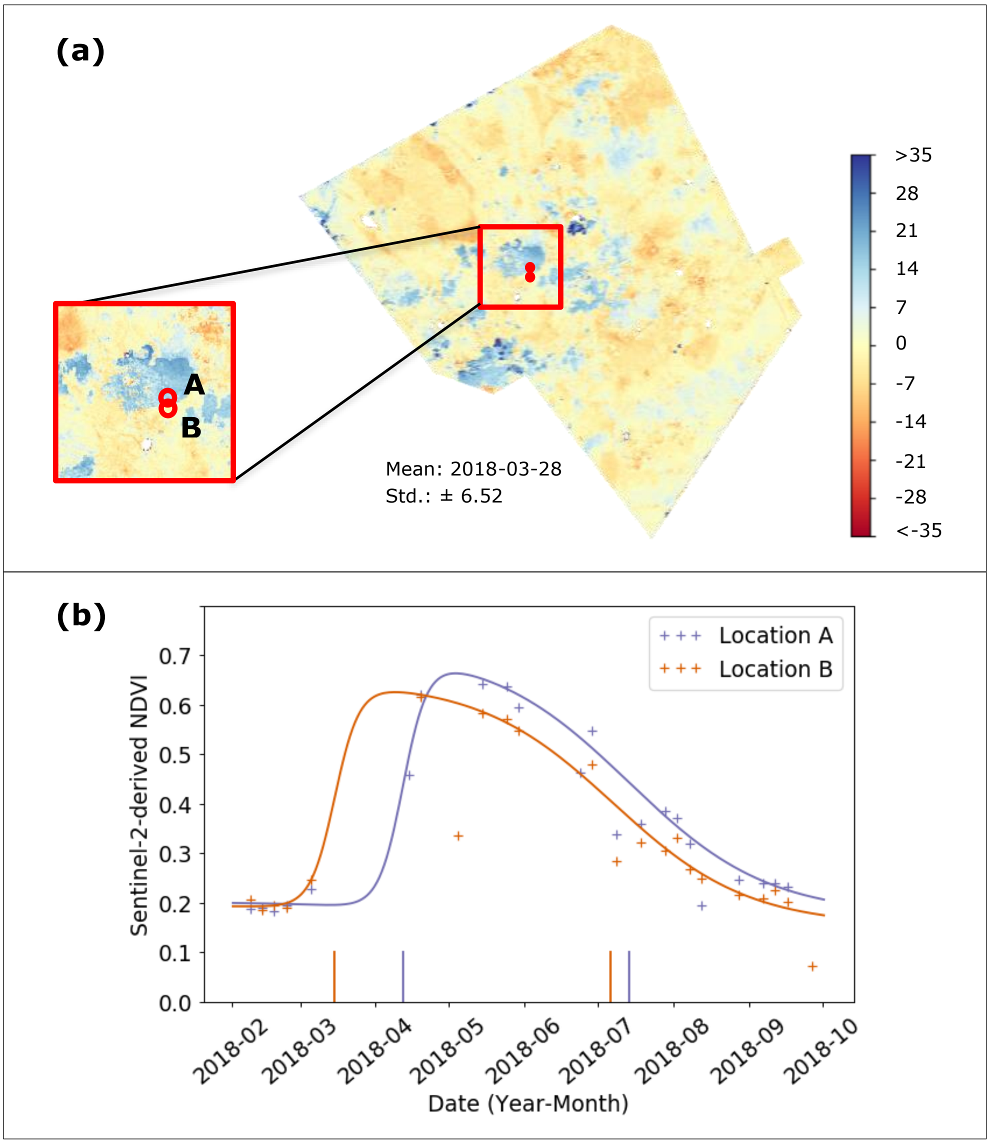

Figure 15: Illustration of the artefacts in Sentinel-2-derived SOS_{50} map for LR2018 (Figure A4b in Appendix). Panel a is the enlarged Sentinel-2-derived SOS_{50} for LR2018. Panel b compares the NDVI time series for location A and location B. As indicated in panel a, location A is a pixel inside the artefact and location B is a pixel near but outside the artefact. In panel b, the vertical lines near x-axis indicate the SOS_{50} and EOS_{50} retrieved from each fitted curve.

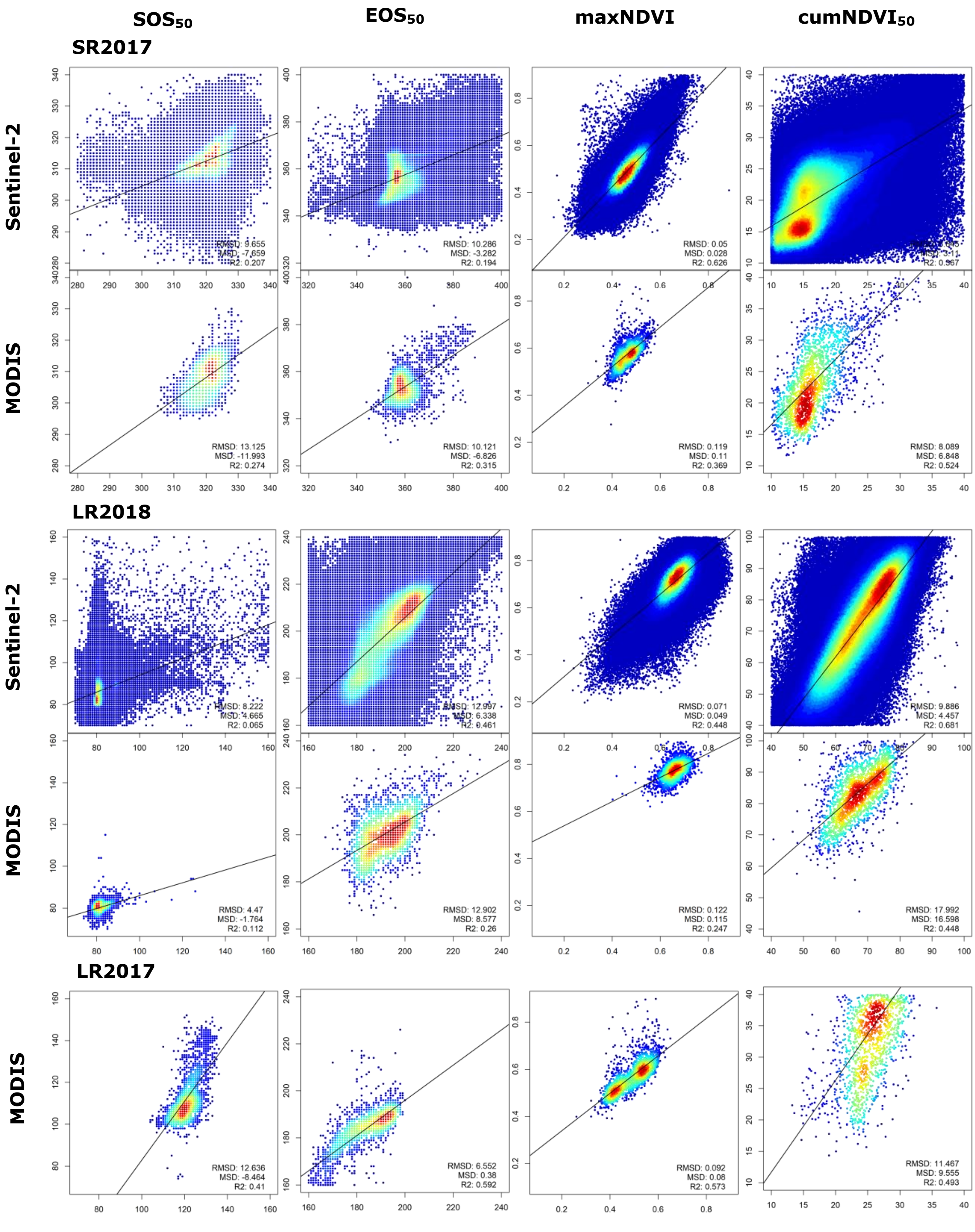

Figure 16: Density scatterplots for SOS_{50}, EOS_{50}, maxNDVI and $cumNDVI_{50}$ per season. The x-axis is the PS-derived phenological metric that had been resampled to 10 or 250 m to match the spatial resolution of the data source indicated on y-axis. The y-axis is the phenological metric derived from Sentinel-2 or MODIS. Blue to red indicates the increase in the frequency. The black line in each plot is the linear regression model. RMSD, MSD and R^2 are reported in each plot.

5.5. Robustness of phenological metrics estimation

Figure 17 illustrates the impact of reduced number of available images on the phenological metric estimates as compared to using the full PS dataset. Unsurprisingly, the increase in the number of observations left out resulted in larger (R)RMSD values for all metrics. The average (R)RMSD had almost a linear relationship with the percentage of missing observations. Specifically, removing 5% of the observations resulted in <4 days difference in SOS_{50} and EOS_{50} as compared to the metrics retrieved from the full NDVI time series. The RMSD increased to ~9 days for SOS_{50} and ~11 days for EOS_{50} when 50% of observations were removed. For $cumNDVI_{50}$, the value of RRMSD was from ~0.06 to ~0.23 with the increase of missing observation from 5% to 50%. The missing observations caused smaller RRMSD in maxNDVI (< 10%) as compared to $cumNDVI_{50}$.

Figure 18 shows the impact of missing observations in a certain period on the estimation of phenological metrics. The lack of observations at the beginning and the very end of the growing seasons both resulted in relatively great impacts on SOS_{50}, e.g. in the second half month in March 2018 (LR2018) (RMSD = 14.21 days) and in September 2017 (LR2017) (RMSD = 6.89 days). However, the lack of observations in most periods had great impacts on EOS_{50} and the greatest impact was caused by the omission of observations at the very end of the growing season, e.g., in the second half of September 2017 (LR2017) (RMSD = 19.44 days). Overall, the impact (RMSD) of missing observations on the estimation of SOS_{50} and EOS_{50} were less than 20 days. The MSD values for SOS_{50} and EOS_{50} indicate that the omission of observations could cause either later or earlier SOS_{50} and EOS_{50} as compared to the estimates derived from full dataset. Reduced image availability will hide or exaggerate some spatial variabilities of SOS_{50} and EOS_{50} as indicated in *Figure 13*. Nevertheless, the impacts (RRMSD) on maxNDVI were usually very small (<15%). The RRMSD values for $cumNDVI_{50}$ were on average larger than for maxNDVI. In other words, the estimation of $cumNDVI_{50}$ was less robust to the reduced image availability than maxNDVI.

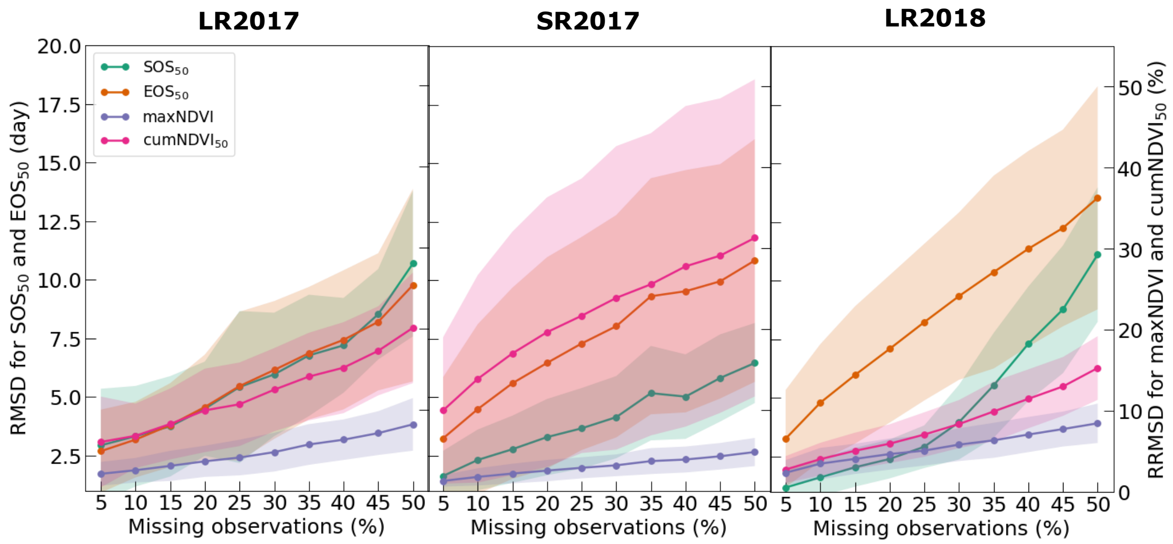

Figure 17: The impact of reduced image availability on the estimation of phenological metrics as compared to using the full PlanetScope dataset. The x-axis shows the percentage of observations that are randomly selected and removed from the original NDVI time series. There were 27 original NDVI time series generated for 24 vegetation samples and three camera locations. Per percentage removed, the random selection of observations and curve fitting were repeated 100 times for each sample NDVI time series. (R)RMSD values were calculated by using the phenological metrics retrieved from original NDVI time series as the base. The point indicates the mean RMSD and the shade around each line indicates the corresponding standard deviation of (R)RMSD for 27 samples.

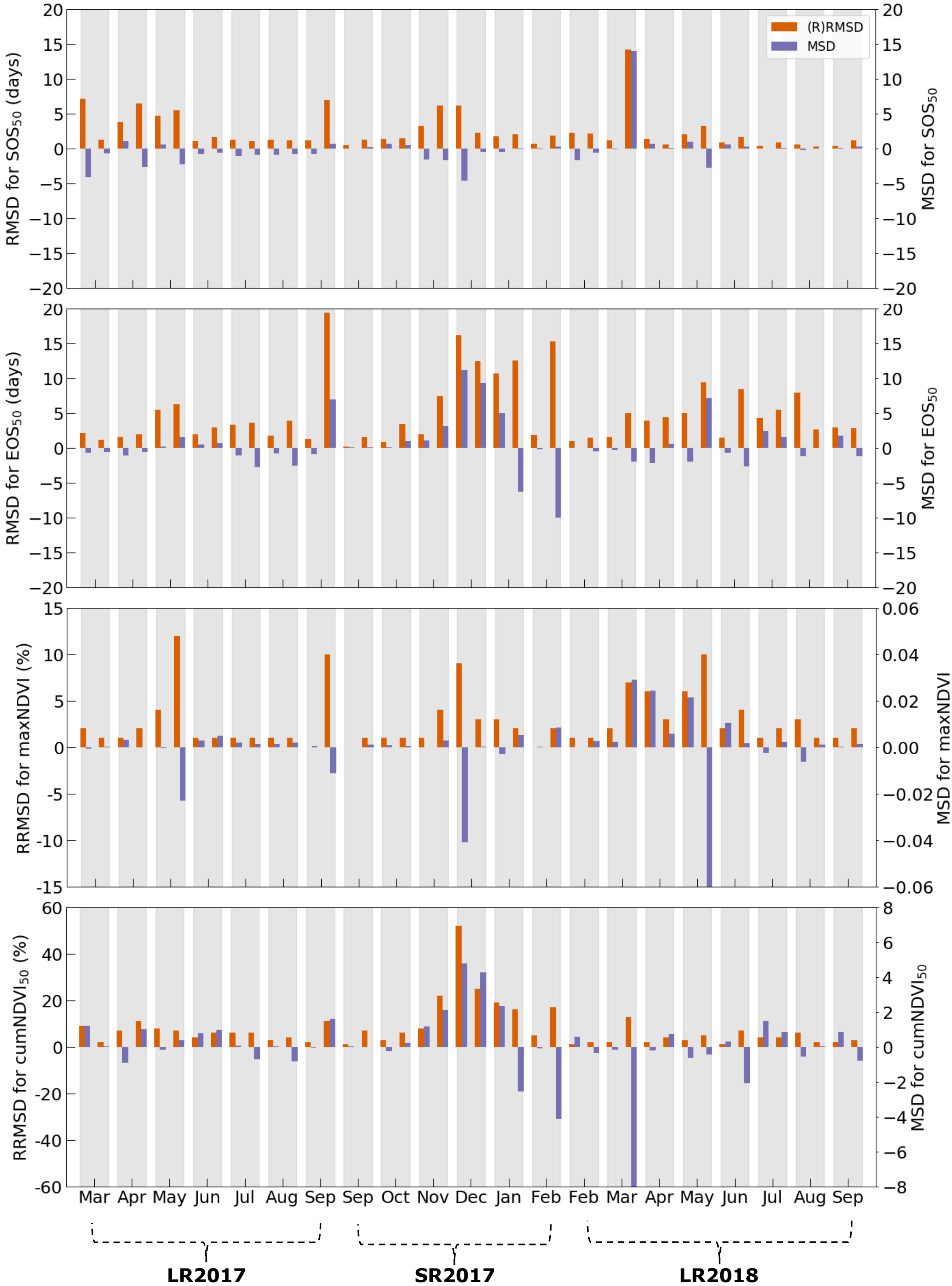

Figure 18: Impact ((R)RMSD and MSD) of removing all observations in the first or second half of a month on phenological metric estimates as compared to the metrics derived from the full PlanetScope dataset.

6. DISCUSSION

The results showed that PS-images are effective to retrieve fine-scale patterns of vegetation phenology for semi-arid rangelands. As compared to camera-based *in-situ* measurements, PS-derived SOS_{50} and EOS_{50} were on average within eight days and 15 days of camera-derived SOS_{50} and EOS_{50}, respectively (*Table 4*). Many phenology-related studies show that the satellite-based temporal phenological metrics have ~10 to 30 days difference from camera-based or visual ground observations (White et al., 2014). These differences can be partially explained by the use of different vegetation indices (Vrieling et al., 2018; Liu et al., 2017). Unlike RGB-based GCC, NDVI uses the reflectance of NIR band, which not only captures the change of chlorophyll but also other signals of green-up and senescence, such as the changes of cell structure. The different viewing angles can also contribute to the inconsistency between satellite- and camera-based phenological metrics. Specifically, the vegetation greenness observed from oblique camera view can be different from the satellites' more nadir view, given that non-photosynthetic elements like stems and grass heads are more dominant in the oblique view (Vrieling et al., 2018). Sentinel-2- and MODIS-derived SOS_{50} and EOS_{50} were also linked to camera-derived equivalents. As *Table 4* summarized, the accuracy of PS-derived SOS_{50} and EOS_{50} was similar to Sentinel-2- and MODIS-derived SOS_{50} and EOS_{50}. Nevertheless, PS-derived NDVI time series show more consistent change patterns with camera-derived GCC time series and daily precipitation records due to the better density of observations (*Figure 12*).

Although PS-derived phenological metrics had disagreements with camera-derived ones, phenological metrics could be estimated for all pixels within the boundary of Kapiti Farm by using a consistent method, which resulted in 3m-resolution phenology maps. These phenology maps (*Figure 13*) showed clear and detailed spatial variations corresponding to differences in land surface (*Figure 1*). These spatial patterns were different across phenological metrics and seasons. Because water availability is the main factor influencing vegetation growth in semi-arid areas (Scholes & Walker, 1993), the spatial differences in phenology are likely a result of variable plant water availability. More rainfall stations across the study area will be helpful for understanding possible spatial variability of rainfall characteristics. Further study is also needed to better understand the effect of soil condition and water-logging caused by uneven topography on the spatial distribution of water availability. PS- and Sentinel-2-derived EOS_{50} map for LR2018 (*Figure 13e-f* and *Figure A3d in Appendix*) showed slight differences between the top and bottom of the hill, which is likely caused by different vegetation cover and water availability. Unsurprisingly, MODIS-derived EOS_{50} map for LR2018 did not show any elevation-derived spatial variabilities in the hill due to its coarse spatial resolution.

Despite the current lack of data for the assessment of driving forces of the spatial and temporal variations of phenology, the spatial patterns of the PS-derived phenology maps are also reflected in Sentinel-2 and MODIS-derived phenology maps (*Figure A4-A7 in Appendix*). Even at the pixel level, PS-derived phenological metrics also have good agreement with Sentinel-2 and MODIS-derived phenological metrics (*Figure 16*). Moreover, due to the finer spatial resolution, PS images can provide more detailed insight into the subtle differences of phenology within a small region and can be easier linked to individual species and ground point measurements (i.e. field camera and flux tower data) than other coarser-resolution images. This could lead to a promising improvement in spatially detailed understanding of semi-arid rangeland ecosystem at the local scale.

Due to the short revisit time of the PS constellation, there was a sufficient number of PS observations over Kapiti Farm for the extraction of vegetation phenology in the three seasons considered (March 2017 to September 2018). However, the simulation analyses showed that if the number of PS observations would be reduced at the beginning or the end of vegetation seasons, this can result in large RMSE values for SOS_{50} and EOS_{50} of up to 20 days (*Figure 18*). Likewise, for Sentinel-2, the lack of cloud-free observation at the beginning of the green-up phase caused the estimation of SOS_{50} to be one-month later, which resulted in apparent artefacts on SOS_{50} map for LR2018 (*Figure 15*). To mitigate the impact of sparse observations on the estimation of phenology, more efforts can be made to improve the robustness of the curve fitting method used in this study. Recently, Jönsson et al. (2018) proposed a so-called robust curve fitting algorithm for Sentinel-2 and Landsat-derived NDVI time series and tested it for a forest in central Sweden. In short, this method defines a reference curve for each pixel based on historical data. If there are no observations in a specific time window, the fitted curve will be adapted to the pre-defined reference curve by constraining some model parameters. Gachoki (2018) has proven the potential and limitations of generating the so-called reference curves by combining multiple years of Landsat observations for Kapiti Farm. Future study is needed to test if this robust curve fitting method can really improve PS-based phenology analysis.

There is also scope to further improve the proposed cloud and cloud shadow detection algorithm. First, the semi-transparent clouds like cirrus can be separated from other cloud types by including other features in the decision tree. For example, the cloud detection algorithm for Sentinel-2 uses Band 10 (1,358 nm-1,388 nm) to detect cirrus (Coluzzi et al., 2018). Even though PS images do not have that band, further analyses may reveal if other integrated spectral or temporal features could be useful for discriminating these cloud types. Secondly, the temporal variations on the series for the various spectral bands can be used to revise the result of pixel-based cloud and cloud shadow detection, which is similar to Multi-Temporal Cloud Detection (MTCD) algorithm proposed by Hagolle et al. (2010). Despite the potential to further improve the cloud and shadow detection, the method developed in this thesis proved capable of accurately eliminating a large number of low-quality observations.

PS images are currently not freely available, except for a limited free availability for research purposes. Following a request to Planet Labs, researchers can download 10,000 km^2 images per month; for multi-temporal acquisitions as needed in this study, this corresponds to a much smaller area. Despite the fact that at present image costs are prohibitive to apply PS time series for phenology assessment for large areas, pilot phenology analyses at the local scale can also provide useful information for understanding ecosystem function and structure, such as the driving forces of spatial and temporal variations of phenology. The finer-resolution phenology products derived from PS, i.e. the maps of SOS, EOS, maxNDVI and cumNDVI, are also expected to be integrated into biodiversity modelling as essential biodiversity variables (Skidmore et al., 2015; Pereira et al., 2013). For example, the cumNDVI as a proxy measurement of gross primary productivity is related to the species richness (Radeloff et al., 2019; Hawkins et al., 2003). Moreover, PS images can also be used as a supplementary or validation data in the phenology analysis based on other data source. Overall, satellite missions that offer frequent fine-resolution optical imagery, such as PS, are an important asset for detailed spatial assessment of vegetation phenology in semi-arid rangelands.

7. CONCLUSION

This study demonstrated the potential of using PS image time series to retrieve fine-resolution vegetation phenology for heterogeneous landscapes with short vegetation seasons, such as semi-arid rangelands. PS-derived SOS_{50} was on average within eight days and EOS_{50} within 15 days of their camera-derived equivalents. Due to higher temporal resolution (~daily), there was a better density of cloud-free observations in PS-based NDVI time series than Sentinel-2-based NDVI time series, as a consequence of which PS-based phenology retrievals were less impacted by the persistent clouds during rainy seasons. Moreover, due to the finer spatial resolution (3m), PS-derived phenology maps showed more spatial details than phenology maps derived from commonly used coarse-resolution sensors like MODIS. The fine-scale patterns that were found in this study demonstrate that PS time series may provide useful inputs for understanding subtle phenological differences and their driving forces. Overall, despite the fact that at present, image costs are prohibitive to apply PS time series for phenology assessment for large areas, PS can achieve spatially detailed phenology analysis for understanding ecosystem function and structure at the local scale, which can contribute to the studies of rangeland management, biodiversity, and wildlife conservation. Still, future efforts can be made for more accurate phenology analysis with PS, including: 1) improving cloud and shadow detection algorithm for PS images, specifically for semi-transparent clouds like cirrus; 2) the development of more robust curve fitting by taking historical vegetation change patterns and precipitation dynamics into consideration.

LIST OF REFERENCES

Abu-Asab, M. S., Peterson, P. M., Shetler, S. G., & Orli, S. S. (2001). Earlier plant flowering in spring as a response to global warming in the Washington, DC, area. *Biodiversity & Conservation*, *10*(4), 597–612. https://doi.org/10.1023/A:1016667125469

Ackerman, S., Strabala, K., Menzel, P., Frey, R., Moeller, C., Gumley, L., … Zhang, H. (1997). *Discriminating clear-sky from cloud with modis algorithm theoretical basis document (mod35)*. Retrieved from http://citeseerx.ist.psu.edu/viewdoc/download?doi=10.1.1.385.7073&rep=rep1&type=pdf

Adole, T., Dash, J., & Atkinson, P. M. (2016). A systematic review of vegetation phenology in Africa. *Ecological Informatics*, *34*, 117–128. https://doi.org/10.1016/J.ECOINF.2016.05.004

Akpo, L.-E. (1997). Phenological interactions between tree and understory herbaceous vegetation of a sahelian semi-arid savanna. *Plant Ecology*, *131*(2), 241–248. https://doi.org/10.1023/A:1009762123397

Bai, T., Li, D., Sun, K., Chen, Y., & Li, W. (2016). Cloud detection for high-resolution satellite imagery using machine learning and multi-feature fusion. *Remote Sensing*, *8*(9), 715. https://doi.org/10.3390/rs8090715

Bailey, S.-A., Horner-Devine, M. C., Luck, G., Moore, L. A., Carney, K. M., Anderson, S., … Fleishman, E. (2004). Primary productivity and species richness: relationships among functional guilds, residency groups and vagility classes at multiple spatial scales. *Ecography*, *27*(2), 207–217. https://doi.org/10.1111/j.0906-7590.2004.03631.x

Beck, P. S. A., Atzberger, C., Høgda, K. A., Johansen, B., & Skidmore, A. K. (2006). Improved monitoring of vegetation dynamics at very high latitudes: A new method using MODIS NDVI. *Remote Sensing of Environment*, *100*(3), 321–334. https://doi.org/10.1016/J.RSE.2005.10.021

Belgiu, M., & Drăguţ, L. (2016). Random forest in remote sensing: a review of applications and future directions. *ISPRS Journal of Photogrammetry and Remote Sensing*, *114*, 24–31. https://doi.org/10.1016/J.ISPRSJPRS.2016.01.011

Bloor, J. M. G., Pichon, P., Falcimagne, R., Leadley, P., & Soussana, J.-F. (2010). Effects of warming, summer drought, and CO2 enrichment on aboveground biomass production, flowering phenology, and community structure in an upland grassland ecosystem. *Ecosystems*, *13*(6), 888–900. https://doi.org/10.1007/s10021-010-9363-0

Champion, N. (2016). Automatic detection of clouds and shadows using high resolution satellite image time series. *The International Archives of the Photogrammetry, Remote Sensing and Spatial Information Sciences*, *XLI-B3*, 475–479. https://doi.org/10.5194/isprsarchives-XLI-B3-475-2016

Chang, J., Ciais, P., Viovy, N., Soussana, J.-F., Klumpp, K., & Sultan, B. (2017). Future productivity and phenology changes in European grasslands for different warming levels: implications for grassland management and carbon balance. *Carbon Balance and Management*, *12*(1), 11. https://doi.org/10.1186/s13021-017-0079-8

Cho, M. A., Ramoelo, A., & Dziba, L. (2017). Response of land surface phenology to variation in tree cover during green-up and senescence periods in the semi-arid savanna of Southern Africa. *Remote Sensing*, *9*(7), 689. https://doi.org/10.3390/rs9070689

Coluzzi, R., Imbrenda, V., Lanfredi, M., & Simoniello, T. (2018). A first assessment of the Sentinel-2 Level 1-C cloud mask product to support informed surface analyses. *Remote Sensing of Environment*, *217*, 426–443. https://doi.org/10.1016/J.RSE.2018.08.009

Cooley, S., Smith, L., Stepan, L., & Mascaro, J. (2017). Tracking dynamic northern surface water changes with high-frequency Planet CubeSat imagery. *Remote Sensing*, *9*(12), 1306. https://doi.org/10.3390/rs9121306

Crimmins, M. A., & Crimmins, T. M. (2008). Monitoring plant phenology using digital repeat photography. *Environmental Management*, *41*(6), 949–958. https://doi.org/10.1007/s00267-008-9086-6

Dahlin, K. M., Ponte, D. Del, Setlock, E., & Nagelkirk, R. (2017). Global patterns of drought deciduous phenology in semi-arid and savanna-type ecosystems. *Ecography*, *40*(2), 314–323. https://doi.org/10.1111/ecog.02443

Didan, K. (2015a). *MOD13A1 MODIS/Terra Vegetation Indices 16-Day L3 Global 500m SIN Grid V006 [Data set]*. NASA EOSDIS LP DAAC. https://doi.org/10.5067/MODIS/MOD13A1.006

Didan, K. (2015b). *MYD13Q1 MODIS/Aqua Vegetation Indices 16-Day L3 Global 250m SIN Grid V006 [Data set]*. NASA EOSDIS LP DAAC. https://doi.org/10.5067/MODIS/MYD13Q1.006

Eilers, P. H. C. (2003). A perfect smoother. *Analytical Chemistry*, *75*(14), 3631–3636. https://doi.org/10.1021/AC034173T
European Space Agency (ESA). (2018). Sentinel Online - ESA. Retrieved August 15, 2018, from https://sentinel.esa.int/web/sentinel/home
Fisher, J. I., Mustard, J. F., & Vadeboncoeur, M. A. (2006). Green leaf phenology at Landsat resolution: Scaling from the field to the satellite. *Remote Sensing of Environment*, *100*(2), 265–279. https://doi.org/10.1016/J.RSE.2005.10.022
Gachoki, S. M. (2018). *Estimating vegetation phenology at 30m resolution with multi- temporal optical imagery for a rangeland site in Kenya* (MSc thesis). University of Twente Faculty of Geo-Information and Earth Observation (ITC), Enschede.
Ghasemian, N., & Akhoondzadeh, M. (2018). Introducing two Random Forest based methods for cloud detection in remote sensing images. *Advances in Space Research*, *62*(2), 288–303. https://doi.org/10.1016/J.ASR.2018.04.030
Gillespie, A. R., Kahle, A. B., & Walker, R. E. (1987). Color enhancement of highly correlated images. II. Channel ratio and "chromaticity" transformation techniques. *Remote Sensing of Environment*, *22*(3), 343–365. https://doi.org/10.1016/0034-4257(87)90088-5
Gong, Z., Kawamura, K., Ishikawa, N., Goto, M., Wulan, T., Alateng, D., … Ito, Y. (2015). MODIS normalized difference vegetation index (NDVI) and vegetation phenology dynamics in the Inner Mongolia grassland. *Solid Earth*, *6*, 1185–1194. https://doi.org/10.5194/se-6-1185-2015
Grossiord, C., Sevanto, S., Adams, H. D., Collins, A. D., Dickman, L. T., McBranch, N., … McDowell, N. G. (2017). Precipitation, not air temperature, drives functional responses of trees in semi-arid ecosystems. *Journal of Ecology*, *105*(1), 163–175. https://doi.org/10.1111/1365-2745.12662
Guan, K., Wood, E. F., Medvigy, D., Kimball, J., Pan, M., Caylor, K. K., … Jones, M. O. (2014). Terrestrial hydrological controls on land surface phenology of African savannas and woodlands. *Journal of Geophysical Research: Biogeosciences*, *119*(8), 1652–1669. https://doi.org/10.1002/2013JG002572
Hagolle, O., Huc, M., Pascual, D. V., & Dedieu, G. (2010). A multi-temporal method for cloud detection, applied to FORMOSAT-2, VENμS, LANDSAT and SENTINEL-2 images. *Remote Sensing of Environment*, *114*(8), 1747–1755. https://doi.org/10.1016/J.RSE.2010.03.002
Hawkins, B. A., Field, R., Cornell, H. V., Currie, D. J., Guégan, J.-F., Kaufman, D. M., … Turner, J. R. G. (2003). Energy, water, and broad-scale geographic patterns of species richness. *Ecology*, *84*(12), 3105–3117. https://doi.org/10.1890/03-8006
Hermance, J. F., Augustine, D. J., & Derner, J. D. (2015). Quantifying characteristic growth dynamics in a semi-arid grassland ecosystem by predicting short-term NDVI phenology from daily rainfall: a simple four parameter coupled-reservoir model. *International Journal of Remote Sensing*, *36*(22), 5637–5663. https://doi.org/10.1080/01431161.2015.1103916
Herrick, J. E., Karl, J. W., McCord, S. E., Buenemann, M., Riginos, C., Courtright, E., … Bestelmeyer, B. (2017). Two New Mobile Apps for Rangeland Inventory and Monitoring by Landowners and Land Managers. *Rangelands*, *39*(2), 46–55. https://doi.org/10.1016/J.RALA.2016.12.003
Heumann, B. W., Seaquist, J. W., Eklundh, L., & Jönsson, P. (2007). AVHRR derived phenological change in the Sahel and Soudan, Africa, 1982–2005. *Remote Sensing of Environment*, *108*(4), 385–392. https://doi.org/10.1016/J.RSE.2006.11.025
Houborg, R., & McCabe, M. (2018). Daily retrieval of NDVI and LAI at 3 m resolution via the fusion of CubeSat, Landsat, and MODIS data. *Remote Sensing*, *10*(6), 890. https://doi.org/10.3390/rs10060890
Hovenden, M. J., Newton, P. C. D., & Wills, K. E. (2014). Seasonal not annual rainfall determines grassland biomass response to carbon dioxide. *Nature*, *511*(7511), 583–586. https://doi.org/10.1038/nature13281
Hovenden, M. J., Wills, K. E., Vander Schoor, J. K., Williams, A. L., & Newton, P. C. D. (2008). Flowering phenology in a species-rich temperate grassland is sensitive to warming but not elevated CO_2. *New Phytologist*, *178*(4), 815–822. https://doi.org/10.1111/j.1469-8137.2008.02419.x
Huete, A., Didan, K., Miura, T., Rodriguez, E. ., Gao, X., & Ferreira, L. . (2002). Overview of the radiometric and biophysical performance of the MODIS vegetation indices. *Remote Sensing of Environment*, *83*(1–2), 195–213. https://doi.org/10.1016/S0034-4257(02)00096-2
Inoue, T., Nagai, S., Kobayashi, H., & Koizumi, H. (2015). Utilization of ground-based digital photography for the evaluation of seasonal changes in the aboveground green biomass and foliage

phenology in a grassland ecosystem. *Ecological Informatics*, *25*, 1–9. https://doi.org/10.1016/J.ECOINF.2014.09.013

International Livestock Research Institute (ILRI). (2018). ILRI's Kapiti livestock research station. Retrieved January 26, 2019, from https://news.ilri.org/2018/01/05/ilris-kapiti-livestock-research-station-and-kenyan-and-global-public-goods-imperiled-by-land-grabs-in-kenya/

IPCC. (2013). *Climate Change 2013 The Physical Science Basis Working Group I Contribution to the Fifth Assessment Report of the Intergovernmental Panel on Climate Change Summary for Policymakers*. (T. F. Stocker, D. Qin, G.-K. Plattner, M. M. B. Tignor, S. K. Allen, J. Boschung, … P. M. Midgley, Eds.). Cambridge, United Kingdom and New York, NY, USA: Cambridge University Press. Retrieved from www.climatechange2013.org.

Irish, R. R., Barker, J. L., Goward, S. N., & Arvidson, T. (2006). Characterization of the Landsat-7 ETM+ Automated Cloud-Cover Assessment (ACCA) algorithm. *Photogrammetric Engineering & Remote Sensing*, *72*(10), 1179–1188. https://doi.org/10.14358/PERS.72.10.1179

Jakubauskas, M. E., Legates, D. R., & Kastens, J. H. (2001). Harmonic analysis of time-series AVHRR NDVI data. *Photogrammetric Engineering and Remote Sensing*, *67*(4), 461–470. Retrieved from https://pdfs.semanticscholar.org/7fb2/fe487764412ef43f1e3793cc0efae4f47d68.pdf

Jentsch, A., Kreyling, J., Boettcher-Treschkow, J., & Beierkuhnlein, C. (2009). Beyond gradual warming: extreme weather events alter flower phenology of European grassland and heath species. *Global Change Biology*, *15*(4), 837–849. https://doi.org/10.1111/j.1365-2486.2008.01690.x

Jolly, W. M., & Running, S. W. (2004). Effects of precipitation and soil water potential on drought deciduous phenology in the Kalahari. *Global Change Biology*, *10*(3), 303–308. https://doi.org/10.1046/j.1365-2486.2003.00701.x

Jönsson, P., Cai, Z., Melaas, E., Friedl, M., Eklundh, L., Jönsson, P., … Eklundh, L. (2018). A Method for Robust Estimation of Vegetation Seasonality from Landsat and Sentinel-2 Time Series Data. *Remote Sensing*, *10*(4), 635. https://doi.org/10.3390/rs10040635

Jonsson, P., & Eklundh, L. (2002). Seasonality extraction by function fitting to time-series of satellite sensor data. *IEEE Transactions on Geoscience and Remote Sensing*, *40*(8), 1824–1832. https://doi.org/10.1109/TGRS.2002.802519

Kääb, A., Altena, B., & Mascaro, J. (2017). Coseismic displacements of the 14 November 2016 Mw 7.8 Kaikoura, New Zealand, earthquake using the Planet optical cubesat constellation. *Natural Hazards and Earth System Sciences*, *17*(5), 627–639. https://doi.org/10.5194/nhess-17-627-2017

Keenan, T. F., Darby, B., Felts, E., Sonnentag, O., Friedl, M. A., Hufkens, K., … Richardson, A. D. (2014). Tracking forest phenology and seasonal physiology using digital repeat photography: a critical assessment. *Ecological Applications*, *24*(6), 1478–1489. https://doi.org/10.1890/13-0652.1

Liu, Y., Hill, M. J., Zhang, X., Wang, Z., Richardson, A. D., Hufkens, K., … Schaaf, C. B. (2017). Using data from Landsat, MODIS, VIIRS and PhenoCams to monitor the phenology of California oak/grass savanna and open grassland across spatial scales. *Agricultural and Forest Meteorology*, *237–238*, 311–325. https://doi.org/10.1016/J.AGRFORMET.2017.02.026

Mathu, W. (2009). *Terminal evaluation of UNEP/GEF project gf/3010-05-10 (4857) – dry land livestock wild life environment interface project (DLWEIP)* (Vol. 10). Retrieved from https://wedocs.unep.org/rest/bitstreams/10708/retrieve

Melaas, E. K., Friedl, M. A., & Zhu, Z. (2013). Detecting interannual variation in deciduous broadleaf forest phenology using Landsat TM/ETM + data. *Remote Sensing of Environment*, *132*, 176–185. https://doi.org/10.1016/J.RSE.2013.01.011

Melaas, E. K., Sulla-Menashe, D., Gray, J. M., Black, T. A., Morin, T. H., Richardson, A. D., & Friedl, M. A. (2016). Multisite analysis of land surface phenology in North American temperate and boreal deciduous forests from Landsat. *Remote Sensing of Environment*, *186*, 452–464. https://doi.org/10.1016/J.RSE.2016.09.014

Meroni, M., Verstraete, M. M., Rembold, F., Urbano, F., & Kayitakire, F. (2014). A phenology-based method to derive biomass production anomalies for food security monitoring in the Horn of Africa. *International Journal of Remote Sensing*, *35*(7), 2472–2492. https://doi.org/10.1080/01431161.2014.883090

Migliavacca, M., Galvagno, M., Cremonese, E., Rossini, M., Meroni, M., Sonnentag, O., … Richardson, A. D. (2011). Using digital repeat photography and eddy covariance data to model grassland phenology and photosynthetic CO2 uptake. *Agricultural and Forest Meteorology*, *151*(10), 1325–1337.

https://doi.org/10.1016/J.AGRFORMET.2011.05.012
Misra, G., Buras, A., Heurich, M., Asam, S., & Menzel, A. (2018). LiDAR derived topography and forest stand characteristics largely explain the spatial variability observed in MODIS land surface phenology. *Remote Sensing of Environment*, *218*, 231–244. https://doi.org/10.1016/J.RSE.2018.09.027
More, J. J. (1978). The Levenberg-Marquardt algorithm: implementation and theory. In *Numerical analysis* (pp. 105–116). Springer, Berlin, Heidelberg. Retrieved from https://link.springer.com/content/pdf/10.1007/BFb0067700.pdf
Newville, M., Stensitzki, T., Allen, D. B., & Ingargiola, A. (2014). LMFIT: Non-Linear Least-Square Minimization and Curve-Fitting for Python¶. https://doi.org/10.5281/ZENODO.11813
Ouled Belgacem, A., & Louhaichi, M. (2013). The vulnerability of native rangeland plant species to global climate change in the West Asia and North African regions. *Climatic Change*, *119*(2), 451–463. https://doi.org/10.1007/s10584-013-0701-z
Pereira, H. M., Ferrier, S., Walters, M., Geller, G. N., Jongman, R. H. G., Scholes, R. J., … Wegmann, M. (2013). Essential Biodiversity Variables. *Science*, *339*(6117), 277–278. https://doi.org/10.1126/science.1229931
Planet Labs Inc. (2018). Planet — Explorer Beta. Retrieved August 14, 2018, from https://www.planet.com/products/explorer/
Planet Team. (2017). Planet — Planet Imagery Products. Retrieved May 25, 2018, from https://www.planet.com/docs/spec-sheets/sat-imagery/
Prevéy, J. S., & Seastedt, T. R. (2014). Seasonality of precipitation interacts with exotic species to alter composition and phenology of a semi-arid grassland. *Journal of Ecology*, *102*(6), 1549–1561. https://doi.org/10.1111/1365-2745.12320
Radeloff, V. C., Dubinin, M., Coops, N. C., Allen, A. M., Brooks, T. M., Clayton, M. K., … Hobi, M. L. (2019). The Dynamic Habitat Indices (DHIs) from MODIS and global biodiversity. *Remote Sensing of Environment*, *222*, 204–214. https://doi.org/10.1016/j.rse.2018.12.009
Reeves, M. C., Moreno, A. L., Bagne, K. E., & Running, S. W. (2014). Estimating climate change effects on net primary production of rangelands in the United States. *Climatic Change*, *126*(3–4), 429–442. https://doi.org/10.1007/s10584-014-1235-8
Richardson, A. D., Jenkins, J. P., Braswell, B. H., Hollinger, D. Y., Ollinger, S. V., & Smith, M.-L. (2007). Use of digital webcam images to track spring green-up in a deciduous broadleaf forest. *Oecologia*, *152*(2), 323–334. https://doi.org/10.1007/s00442-006-0657-z
Scholes, R. J., & Walker, B. H. (1993). *An African savanna : synthesis of the Nylsvley study*. Cambridge University Press. Retrieved from http://agris.fao.org/agris-search/search.do?recordID=GB9523112
Schwartz, M. D. (2013). Introduction. In M. D. Schwartz (Ed.), *Phenology: an integrative environmental science* (2nd ed., pp. 1–5). Dordrecht: Springer Netherlands. https://doi.org/10.1007/978-94-007-6925-0_1
Shen, M., Tang, Y., Chen, J., Zhu, X., & Zheng, Y. (2011). Influences of temperature and precipitation before the growing season on spring phenology in grasslands of the central and eastern Qinghai-Tibetan Plateau. *Agricultural and Forest Meteorology*, *151*(12), 1711–1722. https://doi.org/10.1016/J.AGRFORMET.2011.07.003
Shi, Y., Huang, W., Ye, H., Ruan, C., Xing, N., Geng, Y., … Peng, D. (2018). Partial least square discriminant analysis based on normalized two-stage vegetation indices for mapping damage from rice diseases using PlanetScope datasets. *Sensors*, *18*(6), 1901. https://doi.org/10.3390/s18061901
Skidmore, A. K., Pettorelli, N., Coops, N. C., Geller, G. N., Hansen, M., Lucas, R., … Wegmann, M. (2015). Environmental science: Agree on biodiversity metrics to track from space. *Nature*, *523*(7561), 403–405. https://doi.org/10.1038/523403a
Sonnentag, O., Hufkens, K., Teshera-Sterne, C., Young, A. M., Friedl, M., Braswell, B. H., … Richardson, A. D. (2012). Digital repeat photography for phenological research in forest ecosystems. *Agricultural and Forest Meteorology*, *152*, 159–177. https://doi.org/10.1016/J.AGRFORMET.2011.09.009
Sparks, T. H., & Menzel, A. (2002). Observed changes in seasons: an overview. *International Journal of Climatology*, *22*(14), 1715–1725. https://doi.org/10.1002/joc.821
Tseng, D.-C., Tseng, H.-T., & Chien, C.-L. (2008). Automatic cloud removal from multi-temporal SPOT images. *Applied Mathematics and Computation*, *205*(2), 584–600. https://doi.org/10.1016/J.AMC.2008.05.050
Vrieling, A., Meroni, M., Darvishzadeh, R., Skidmore, A. K., Wang, T., Zurita-Milla, R., … Paganini, M. (2018). Vegetation phenology from Sentinel-2 and field cameras for a Dutch barrier island. *Remote*

Sensing of Environment. https://doi.org/10.1016/J.RSE.2018.03.014
Vrieling, A., Skidmore, A. K., Wang, T., Meroni, M., Ens, B. J., Oosterbeek, K., … Paganini, M. (2017). Spatially detailed retrievals of spring phenology from single-season high-resolution image time series. *International Journal of Applied Earth Observation and Geoinformation*, *59*, 19–30. https://doi.org/10.1016/J.JAG.2017.02.021
White, K., Pontius, J., & Schaberg, P. (2014). Remote sensing of spring phenology in northeastern forests: A comparison of methods, field metrics and sources of uncertainty. *Remote Sensing of Environment*, *148*, 97–107. https://doi.org/10.1016/J.RSE.2014.03.017
White, M. A., Thornton, P. E., & Running, S. W. (1997). A continental phenology model for monitoring vegetation responses to interannual climatic variability. *Global Biogeochemical Cycles*, *11*(2), 217–234. https://doi.org/10.1029/97GB00330
Woebbecke, D. M., Meyer, G. E., Bargen, K. Von, & Mortensen, D. A. (1995). Color indices for weed identification under various soil, residue, and lighting conditions. *Transactions of the ASAE*, *38*(1), 259–269. https://doi.org/10.13031/2013.27838
Yu, F., Price, K. P., Ellis, J., & Shi, P. (2003). Response of seasonal vegetation development to climatic variations in eastern central Asia. *Remote Sensing of Environment*, *87*(1), 42–54. https://doi.org/10.1016/S0034-4257(03)00144-5
Zelikova, T. J., Williams, D. G., Hoenigman, R., Blumenthal, D. M., Morgan, J. A., & Pendall, E. (2015). Seasonality of soil moisture mediates responses of ecosystem phenology to elevated CO_2 and warming in a semi-arid grassland. *Journal of Ecology*, *103*(5), 1119–1130. https://doi.org/10.1111/1365-2745.12440
Zhang, J., Feng, L., & Yao, F. (2014). Improved maize cultivated area estimation over a large scale combining MODIS–EVI time series data and crop phenological information. *ISPRS Journal of Photogrammetry and Remote Sensing*, *94*, 102–113. https://doi.org/10.1016/J.ISPRSJPRS.2014.04.023
Zhang, X., Wang, J., Gao, F., Liu, Y., Schaaf, C., Friedl, M., … Henebry, G. M. (2017). Exploration of scaling effects on coarse resolution land surface phenology. *Remote Sensing of Environment*, *190*, 318–330. https://doi.org/10.1016/J.RSE.2017.01.001
Zhu, Z., & Woodcock, C. E. (2012). Object-based cloud and cloud shadow detection in Landsat imagery. *Remote Sensing of Environment*, *118*, 83–94. https://doi.org/10.1016/J.RSE.2011.10.028

Appendix

Table A1: The location of field cameras installed in Kapiti Farm

ID	Latitude	longitude	altitude	Description
KE01	1°35'46.97"S	37° 7'57.91"E	1632	Grassland
KE02	1°35'56.92"S	37° 7'58.01"E	1636	Mixed grass and shrub (acacia drepanolobium)
KE03	1°37'59.04"S	37° 8'9.88"E	1723	Grass and trees (acacia species)

Table A2: The details of field cameras and photos

Property	Value
Camera	
Camera maker	BUSHNELL
F-stop	f/2.8
ISO speed	ISO-100
Max aperture	2.8
Metering mode	Average
Flash mode	No flash
Light source	Daylight
Exposure program	Aperture Priority
Image	
Dimensions	2592 x 1944
Resolution	96 dpi
Bit depth	24
Resolution unit	2
Colour representation	sRGB
Compressed bits/pixel	1.599

Table A3: Vegetation cover in Kapiti Farm

Vegetation community	LandPKS estimates (%)				
	Grass	Shrubs	Trees	Litter	Soil
Acacia shrubland	32.83	18.08	0.00	22.43	26.66
Grassland	38.00	0.00	0.00	26.79	35.20
Woodland	20.33	1.61	24.49	19.00	34.57
Diverse shrubland	32.21	16.79	0.00	20.52	30.49

Table A4: Band math formulas and textural features formulas used for the construction of feature spaces

Name	**Formula**
Spectral features (RGB and NIR, 5 vegetation indices and 42 band math**)**	
Single band	$f(a) = a$
Normalized Difference Vegetation Index	$NDVI = \frac{(NIR - R)}{(NIR + R)}$
Enhanced Vegetation Index	$EVI = \frac{2.5 \times (NIR - R)}{(NIR + 6 \times R - 7.5 \times B + 1)}$
Green Leaf Index	$GLI = \frac{(2 \times G - R - B)}{(2 \times G + R + B)}$
Soil Adjusted Vegetation Index	$SAVI = \frac{(1+L)\times(NIR-R)}{(NIR+R+L)} \quad (L = 0.5)$
Visible Atmospherically Resistance Index	$VARI = \frac{(G - R)}{(G + R - B)}$
Difference	$f(a,b) = a - b$
Ratio	$f(a,b) = a/b$
Depth	$f(a,b) = \frac{a+b}{c}$
Index	$f(a,b) = \frac{a-b}{a+b}$
Index_{-}^{F}	$f(a,b,c,d) = \frac{a-b}{c+d}$
Index_{+}^{F}	$f(a,b,c,d) = \frac{a+b}{c-d}$
Spatial (texture) features (calculate for each band separately, results in 4*18 spatial features)	
Angular second moment i.e. Image uniformity	$ASM = \sum_{i=1}^{L}\sum_{j=1}^{L}\{\hat{P}(i,j)\}^2$
Contrast i.e. Indicate the presence of edges and noise	$cont = \sum_{i=0}^{L-1}(i-j)^2\sum_{i=1}^{L}\sum_{j=1}^{L}\hat{P}(i,j)$
Correlation i.e. Linear correlation of spectral information.	$cor = \sum_{i=0}^{L-1}\sum_{j=0}^{L-1}\frac{(i,j)\hat{P}(i,j) - \mu_x\mu_y)}{\sigma_x\sigma_y}$
Variance i.e. Scattering of spectral information distribution	$var = \sum_{i=0}^{L-1}\sum_{j=0}^{L-1}(i-\mu)^2\hat{P}(i,j)$
Sum variance	$svar = \sum_{i=0}^{2L-2}(i - sent)^2\,\hat{P}_{x+y}(i)$
Difference variance	$dvar = variance\ of\ \hat{P}_{x-y}$
Entropy i.e. Degree of randomness among pixels	$ent = -\sum_{i=0}^{L-1}\sum_{j=0}^{L-1}\hat{P}(i,j)\,log\big[\hat{P}(i,j)\big]$
Sum entropy	$sent = -\sum_{i=0}^{2L-2}\hat{P}_{x+y}(i)\,log\big[\hat{P}_{x+y}(i)\big]$
Difference entropy	$dent = -\sum_{i=0}^{L-1}\hat{P}_{x+y}(i)\log\big[\hat{P}_{x+y}(i)\big]$

Dissimilarity i.e. Local spectral information variations	$dis = \sum_{i=0}^{L-1}\sum_{j=0}^{L-1} \lvert i-j \rvert \hat{P}(i,j)$
Sum Average	$savg = \sum_{i=0}^{2L-2} i\hat{P}_{x+y}(i)$
Inverse Difference Moment	$idm = \sum_{i=0}^{L-1}\sum_{j=0}^{L-1} \frac{1}{1+(i-j)^2}\hat{P}(i,j)$
Information measures of correction 1	$imcorr1 = \frac{HXY - HXY1}{max\{HX, HY\}}\ where,$ $HXY = -\sum_{i=0}^{L-1}\sum_{j=0}^{L-1} \hat{P}(i,j)\, log\left[\hat{P}(i,j)\right]$ $HXY1 = -\sum_{i=0}^{L-1}\sum_{j=0}^{L-1} \hat{P}(i,j)\, log\left[\hat{P}_x(i)\hat{P}_y(j)\right]$ HX and HY are entropies of $\hat{P}_x\ and\ \hat{P}_y$
Information measures of correction 2	$imcorr2 = \left(1 - e^{\lvert -2.0(HXY2 - HXY)\rvert}\right)^{\frac{1}{2}}, where$ $HXY2 = -\sum_{i=0}^{L-1}\sum_{j=0}^{L-1} \hat{P}_x(i)\hat{P}_y(j)\, log\left[\hat{P}_x(i)\hat{P}_y(j)\right]$
Maximal correlation coefficient	$(Secondlargesteigenvalueof Q)^{\frac{1}{2}}\ where$ $Q(i,j) = \sum_{k=0}^{L-1} \frac{\hat{P}(i,k)\hat{P}(j,k)}{\hat{P}_x(i)\hat{P}_y(k)}$
Inertia	$inertia = \sum_{i=0}^{L-1}\sum_{j=0}^{L-1} (i-j)^2\, \hat{P}(i,j)$
Cluster prominence	$prom = \sum_{i=0}^{L-1}\sum_{j=0}^{L-1} (i + j - \mu_i - \mu_j)^4\, \hat{P}(i,j)$
Cluster shade	$shade(\delta, T) = \sum_{i=0}^{L-1}\sum_{j=0}^{L-1} (i + j - \mu_i - \mu_j)^3\, s(i,j,\delta,T)$
Temporal feature	
Time	month (when the image was acquired)

* Where $\hat{P}$ is the value in normalized gray tone matrix; *(i, j)* is the spatial coordinate; *L* is the number of gray levels

Table A5: Monthly thresholds of clear pixels in b2, b2_savg, b4, and b4_savg

Date	b2	b2_savg	b4	b4_savg
2017-3	661, 1474	1326, 2934	1635, 2925	3277, 5830
2017-4	789, 2732	1585, 5461	1829, 4018	3663, 8031
2017-5	413, 1681	833, 3337	1899, 3627	3808, 7237
2017-6	681, 2076	1372, 4140	2095, 4250	4203, 8483
2017-7	656, 1757	1318, 3507	1814, 3167	3635, 6318
2017-8	698, 1640	1401, 3257	1658, 3141	3323, 6262
2017-9	756, 1782	1518, 3541	1688, 3201	3382, 6382
2017-10	648, 1725	1303, 3431	1618, 3164	3243, 6303
2017-11	623, 2581	1248, 5156	1708, 4243	3418, 8467
2017-12	719, 1733	1442, 3451	1943, 3361	3892, 6708
2018-1	672, 1716	1349, 3407	1592, 3356	3187, 6691
2018-2	781, 1962	1569, 3901	1668, 3411	3340, 6802
2018-3	453, 1602	943, 2918	1765, 3265	3635, 7355
2018-4	639, 1356	1280, 2669	2197, 4042	4398, 8055
2018-5	417, 1688	842, 2462	2532, 5613	5080, 9532
2018-6	528, 1591	1061, 3172	2566, 5330	5144, 10650
2018-7	542, 1422	1091, 2812	2579, 5022	5175, 10038
2018-8	687, 1940	1379, 3851	2172, 4014	4355, 8014
2018-9	685, 1555	1374, 3095	1941, 3149	3890, 6287

Table A6: SOS_{50} and EOS_{50} retrieved from camera- and satellite-derived VI time series and per season. The highlighted values are DOY in 2018. The rest values are the DOY in 2017. The values in the brackets are the number of days counted from 1 January 2017.

		SR2017				LR2018			
		Camera	**PS**	**Sentinel-2**	**MODIS**	**Camera**	**PS**	**Sentinel-2**	**MODIS**
SOS_{50}	**KE01**	311	330	309	306	75	79	84	83
	KE02	308	319	306	307	80	76	86	83
	KE03	307	310	314	298	70	75	89	78
EOS_{50}	**KE01**	350	356	359	351	169	190	194	198
	KE02	7 (372)	355	352	351	173	179	205	202
	KE03	358	24 (389)	343	11 (376)	186	181	185	205

Table A7: Impact of the lack of observations in the first or second half of a month on phenological metrics estimations as compare to real metrics derived from original datasets. The impact were quantified by MSD, (R)RMSD. The blueish colour means negative values and the reddish colour means positive values. The higher saturation of reddish and blueish colour indicates larger positive value and lower negative value. nImages refers to the average number of observations in NDVI time series. #Images is the average number of cloud-free observations per fit.

Season	Month	#Images	MSD				RMSD (days)		RRMSD (%)	
			SOS_{50}	EOS_{50}	maxNDVI	$cumNDVI_{50}$	SOS_{50}	EOS_{50}	maxNDVI	$cumNDVI_{50}$
LR2017	Mar.	29	-4.11	-0.74	-0.0008	1.19	7.13	2.13	1.66%	8.86%
		32	-0.74	-0.63	0.0002	0.02	1.25	1.11	0.52%	1.90%
	Apr.	30	1.07	-1.07	0.0030	-0.92	3.76	1.55	1.22%	7.36%
		30	-2.67	-0.59	0.0000	1.02	6.47	1.96	1.81%	11.12%
	May.	30	0.52	0.19	-0.0003	-0.18	4.63	5.42	3.80%	7.54%
		30	-2.33	1.56	-0.0230	0.38	5.44	6.20	11.91%	6.93%
	Jun.	31	-0.81	0.44	0.0029	0.79	1.05	1.91	0.86%	3.61%
		29	-0.59	0.70	0.0049	0.99	1.63	2.90	1.46%	6.41%
	Jul.	29	-1.07	-1.11	0.0021	0.06	1.26	3.28	1.02%	6.26%
		30	-0.89	-2.78	0.0014	-0.70	1.02	3.62	0.63%	5.77%
	Aug.	31	-0.96	-0.81	0.0015	0.05	1.28	1.72	1.20%	2.94%
		27	-0.81	-2.63	0.0020	-0.83	1.15	3.86	0.97%	4.49%
	Sep.	32	-0.81	-0.89	0.0005	-0.04	1.15	1.25	0.39%	1.88%
		29	0.63	6.96	-0.0113	1.61	6.89	19.44	10.22%	11.46%
	Oct.	32	-0.85	-0.67	0.0003	0.06	1.17	1.09	0.32%	2.32%
SR2017	Sep.	40	-0.04	0.04	-0.0001	0.03	0.43	0.19	0.11%	1.19%
		37	0.15	0.11	0.0010	-0.01	1.28	1.55	0.57%	7.14%
	Oct.	37	0.67	0.04	0.0008	-0.23	1.33	0.88	0.56%	3.50%
		37	0.41	0.93	0.0006	0.22	1.40	3.39	0.70%	5.99%
	Nov.	39	-1.63	1.04	-0.0001	1.17	3.22	1.96	1.05%	7.52%
		35	-1.70	3.11	0.0029	2.12	6.12	7.44	4.00%	21.79%
	Dec.	35	-4.63	11.15	-0.0410	4.78	6.13	16.12	8.79%	52.26%
		36	-0.48	9.30	0.0002	4.28	2.20	12.42	2.61%	24.87%
	Jan.	37	-0.48	4.96	-0.0030	2.35	1.69	10.66	2.90%	18.61%
		33	-0.11	-6.30	0.0052	-2.56	2.06	12.54	2.35%	15.64%
	Feb.	35	-0.11	-0.26	0.0001	-0.07	0.64	1.84	0.36%	4.95%
		34	0.30	-10.00	0.0084	-4.14	1.81	15.29	2.19%	17.40%
	Mar.	39	0.04	-1.33	0.0012	-0.51	0.88	1.94	0.55%	5.31%
LR2018	Feb.	38	-1.74	0.00	0.0000	0.58	2.24	0.98	0.79%	1.47%
		38	-0.59	-0.52	0.0025	-0.37	2.11	1.44	1.17%	1.94%
	Mar.	41	-0.11	-0.33	0.0022	-0.16	1.17	1.50	2.06%	1.67%
		39	14.00	-2.00	0.0291	-8.83	14.21	4.97	7.28%	12.71%
	Apr.	41	0.63	-2.15	0.0242	-0.21	1.32	3.88	6.20%	2.08%
		42	0.11	0.59	0.0058	0.72	0.51	4.34	3.39%	3.74%
	May.	40	0.96	-2.00	0.0215	-0.64	2.00	4.94	6.24%	2.96%
		39	-2.74	7.15	-0.0618	-0.43	3.20	9.39	10.34%	5.08%
	Jun.	40	0.56	-0.70	0.0106	0.32	0.88	1.48	2.28%	1.32%
		40	0.22	-2.70	0.0017	-2.09	1.59	8.39	3.98%	7.47%
	Jul.	41	-0.07	2.41	-0.0025	1.49	0.38	4.24	0.92%	3.75%
		41	0.07	1.52	0.0023	0.86	0.86	5.49	1.70%	4.03%
	Aug.	38	-0.26	-1.26	-0.0064	-0.54	0.58	7.92	2.74%	6.40%
		41	0.00	-0.04	0.0012	0.04	0.27	2.59	0.51%	2.07%
	Sep.	36	0.07	1.70	0.0002	0.85	0.38	2.92	0.50%	2.35%
		39	0.22	-1.22	0.0015	-0.81	1.19	2.78	1.73%	3.31%
	Oct.	41	-0.07	-1.19	-0.0035	-0.76	0.27	2.36	1.20%	2.00%

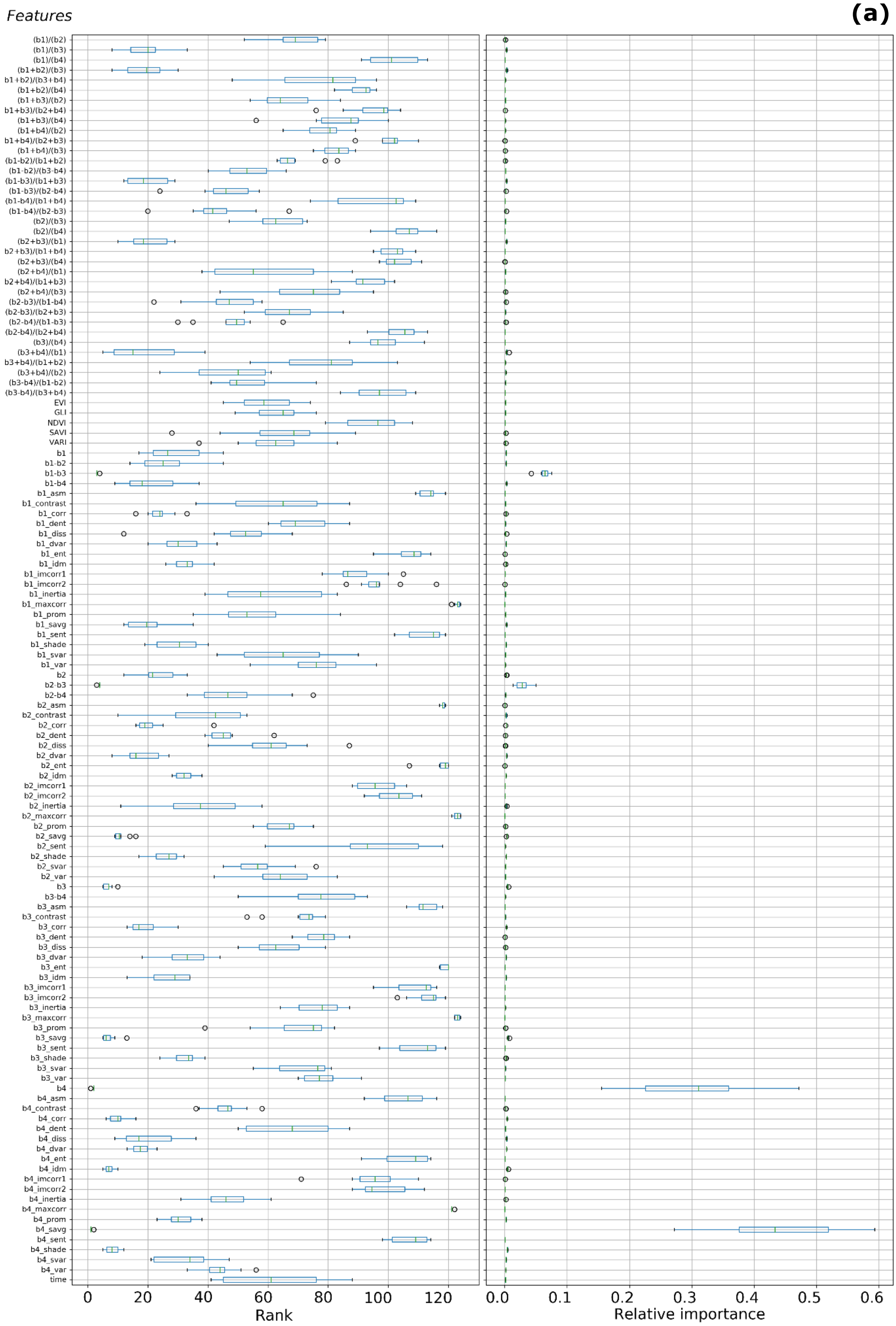
Features
(a)
Rank
Relative importance

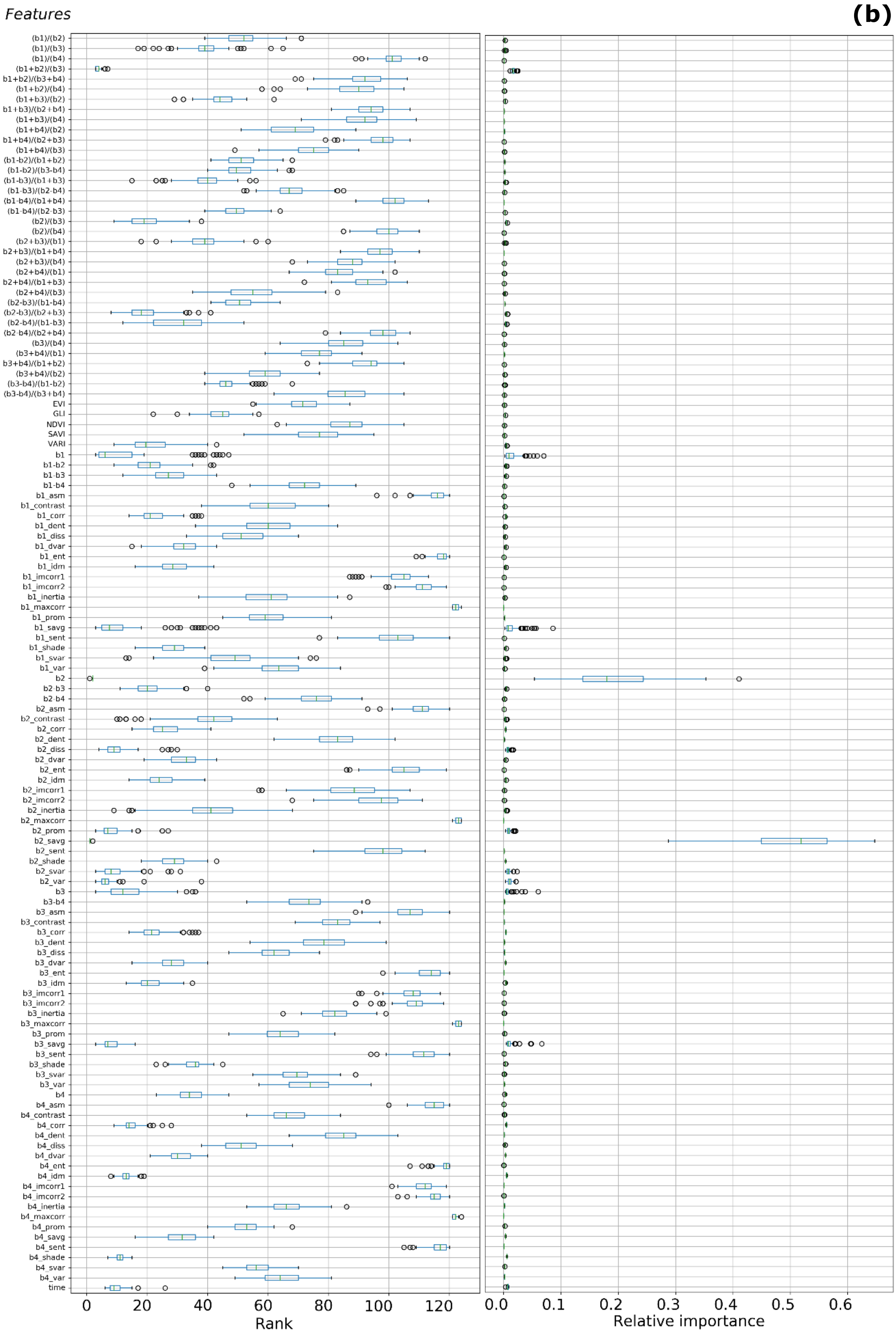

Figure A1: Ranks and values of feature importance of 124 features used for Random Forest-based (a) cloud classification and (b) shadow classification in 100 runs. The feature importance are relative values scaled from 0 to 1, and the higher values represent more contribution to the classification.

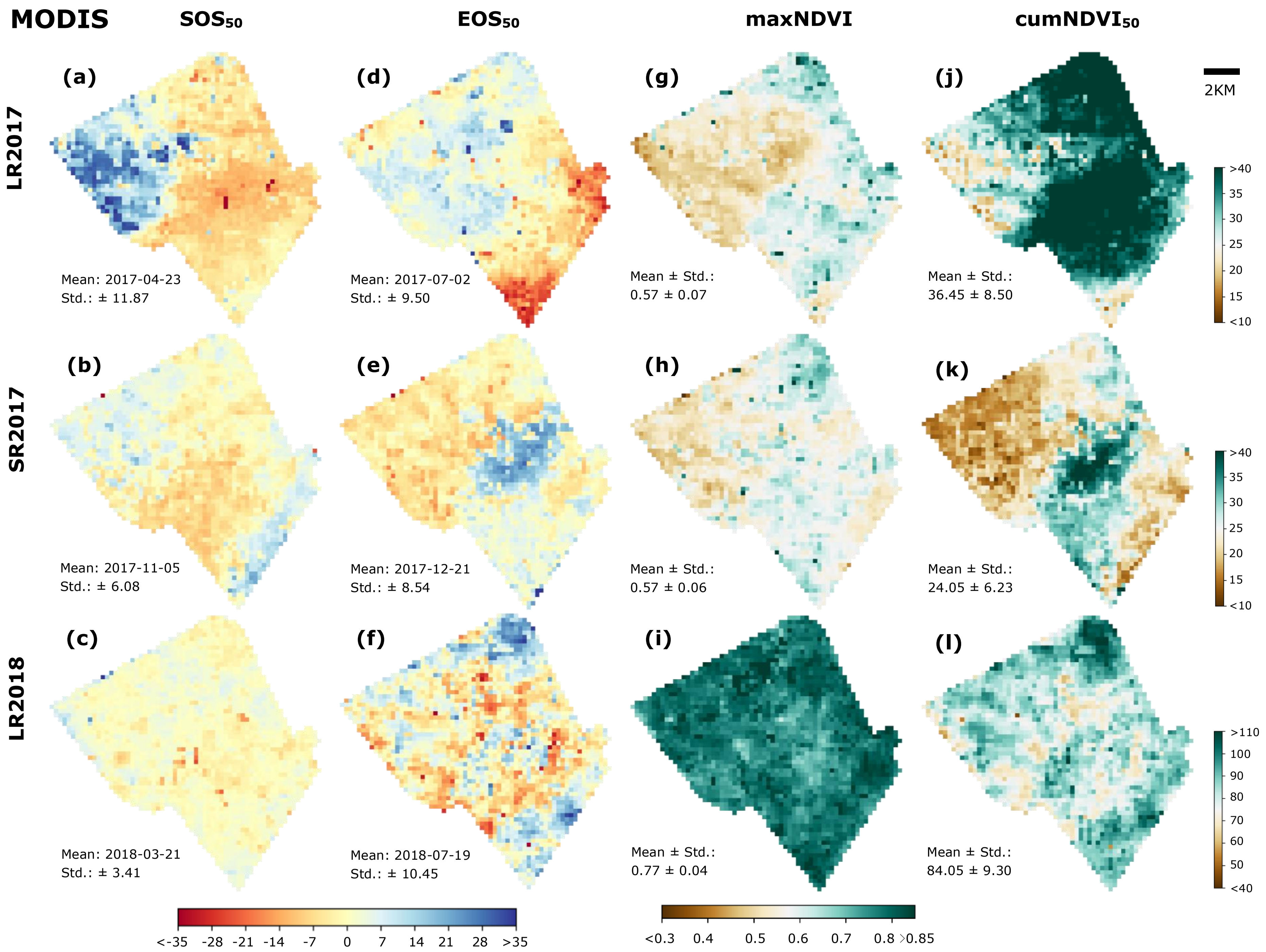

Figure A2: SOS_{50}, EOS_{50}, maxNDVI and $cumNDVI_{50}$ retrieved from MODIS-derived NDVI time series for Kapiti Farm and per seasons. SOS_{50} and EOS_{50} maps in each season are visualized by showing the difference from the mean. Red colours means that the date is before the mean, and blue colours mean that the date is after the mean.

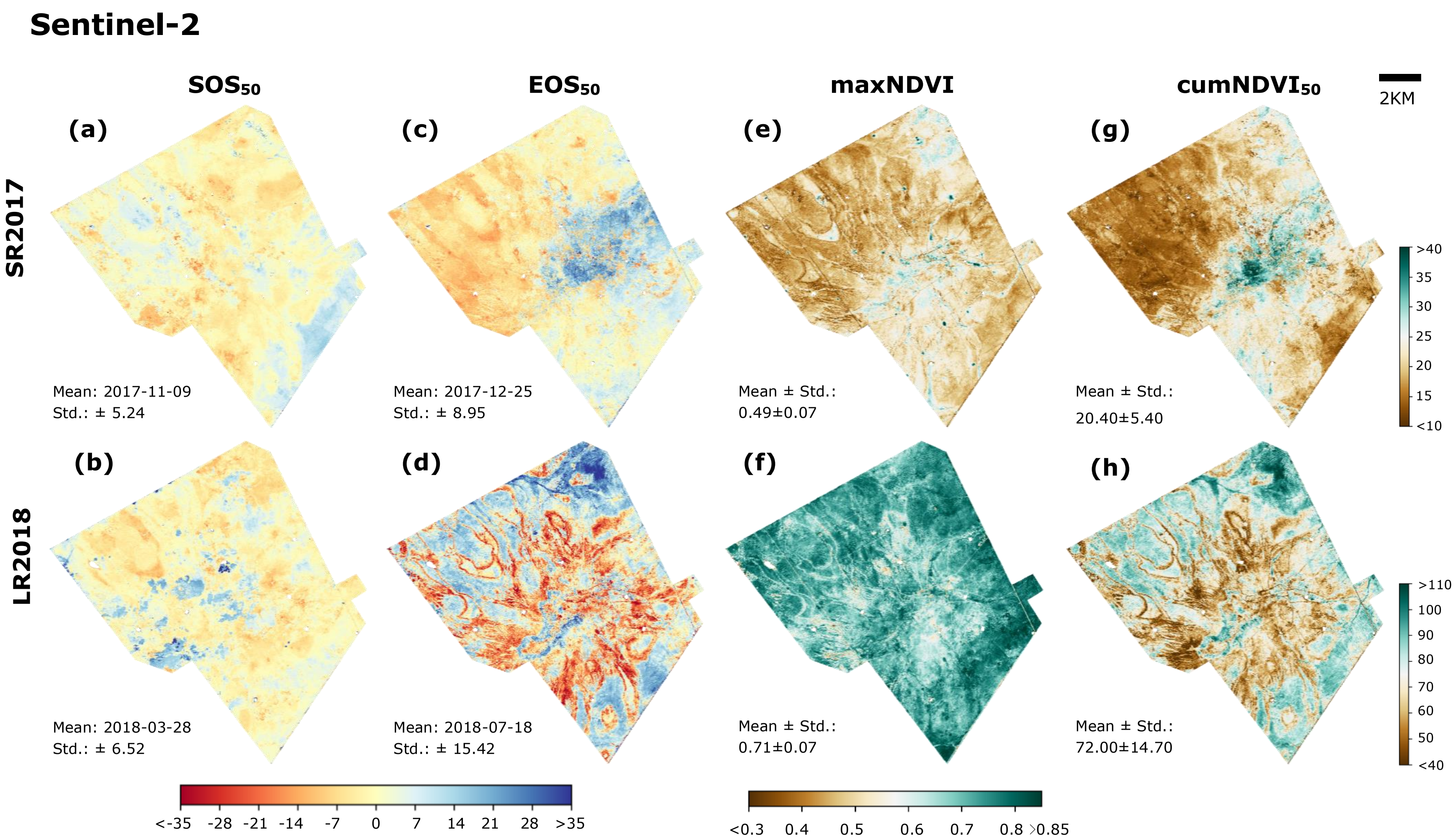

Figure A3: SOS_{50}, EOS_{50}, maxNDVI and cum$NDVI_{50}$ retrieved from Sentinel-2-derived NDVI time series for Kapiti Farm and per seasons. The mean and standard deviation are reported beside each map. SOS_{50} and EOS_{50} maps in each season are visualized by showing the difference from the mean. Red colours means that the date is before the mean, and blue colours mean that the date is after the mean.

SOS_{50}

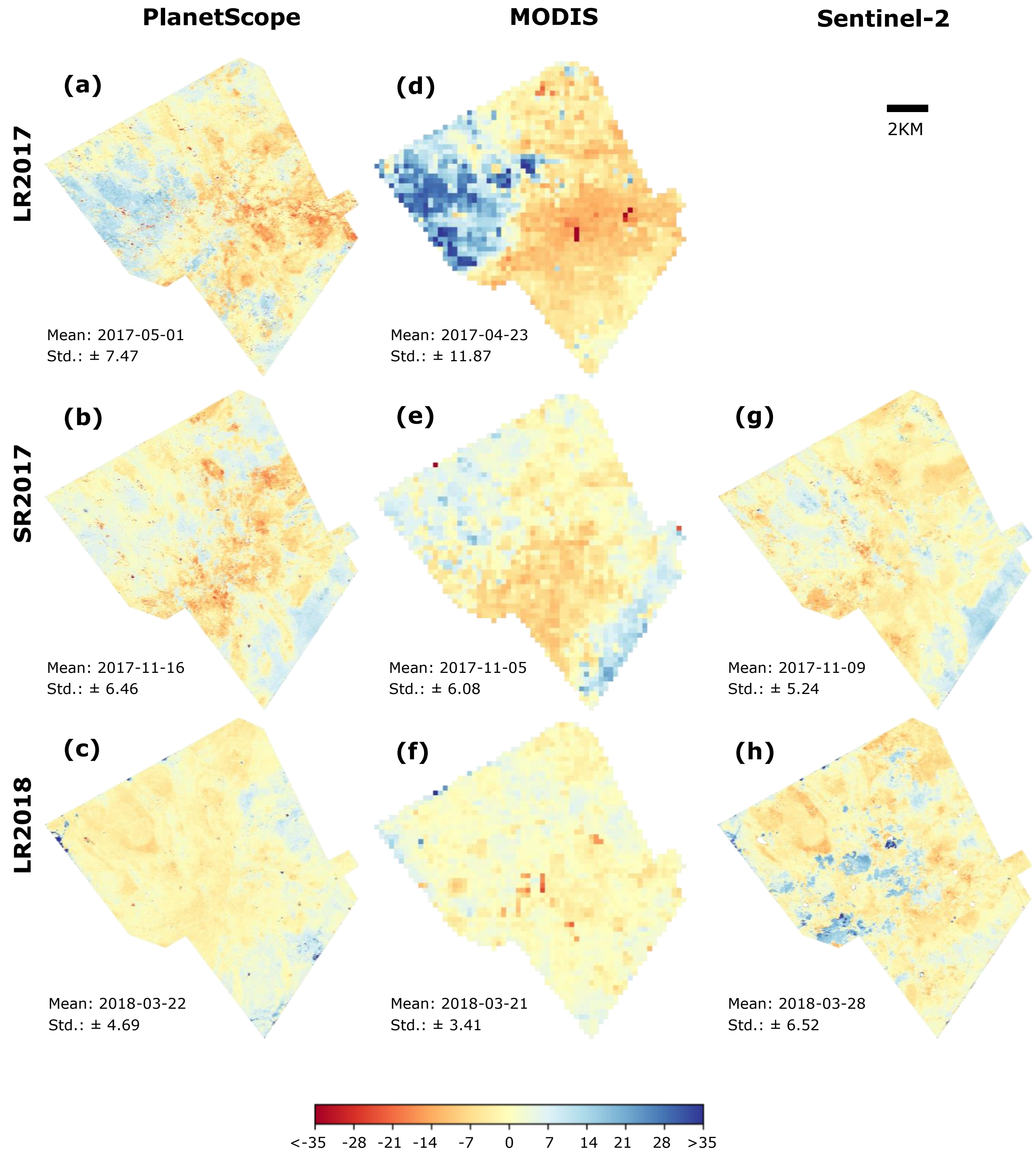

Figure A4: SOS_{50} retrieved from PS, MODIS and Sentinel-2-derived NDVI time series for Kapiti Farm and per seasons. The mean and standard deviation are reported beside each map. All maps are visualized by showing the difference from the mean. Red colours means that the date is before the mean, and blue colours mean that the date is after the mean.

EOS_{50}

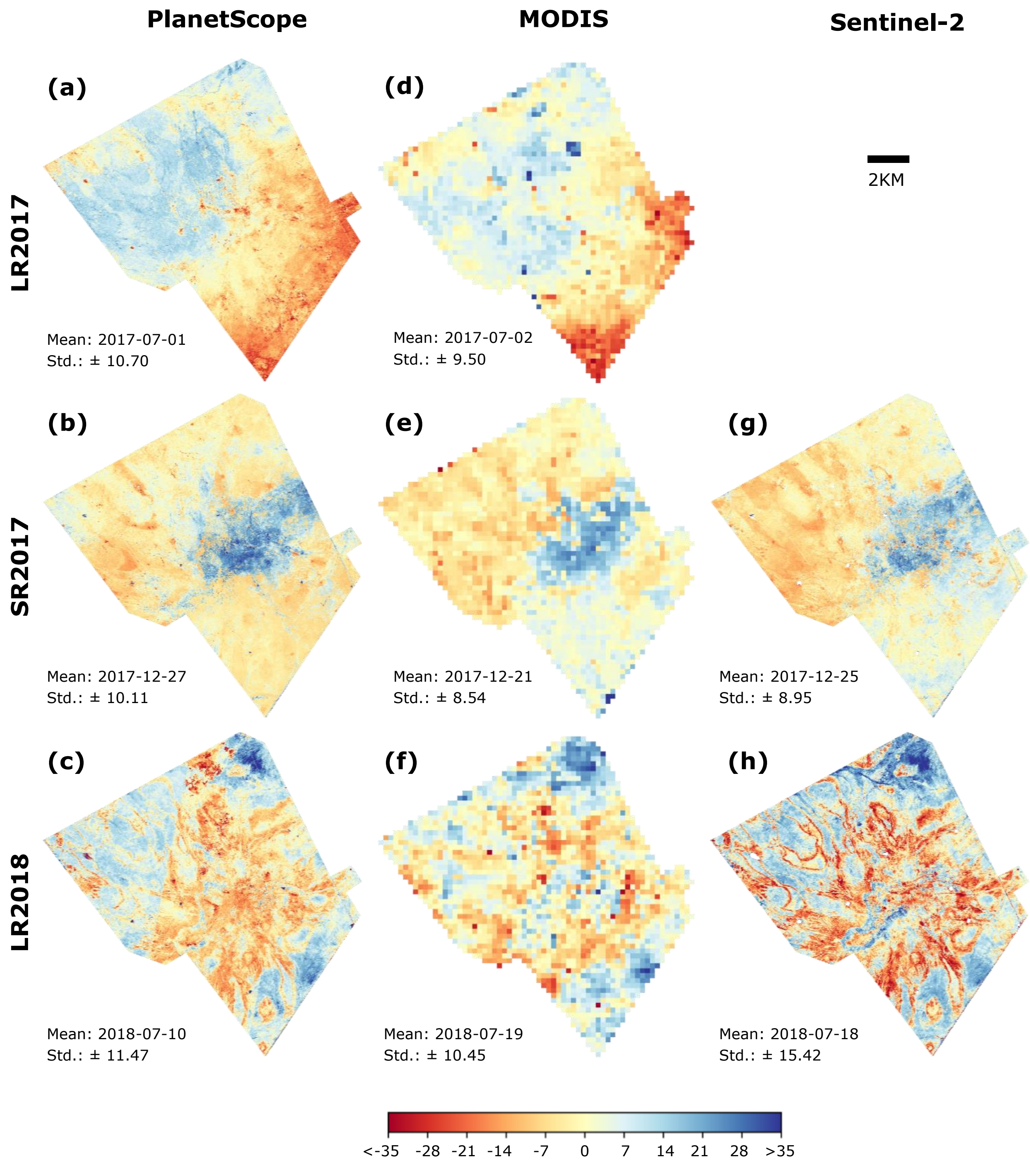

Figure A5: EOS_{50} retrieved from PS, MODIS and Sentinel-2-derived NDVI time series for Kapiti Farm and per seasons. The mean and standard deviation are reported beside each map. All maps are visualized by showing the difference from the mean. Red colours means that the date is before the mean, and blue colours mean that the date is after the mean.

maxNDVI

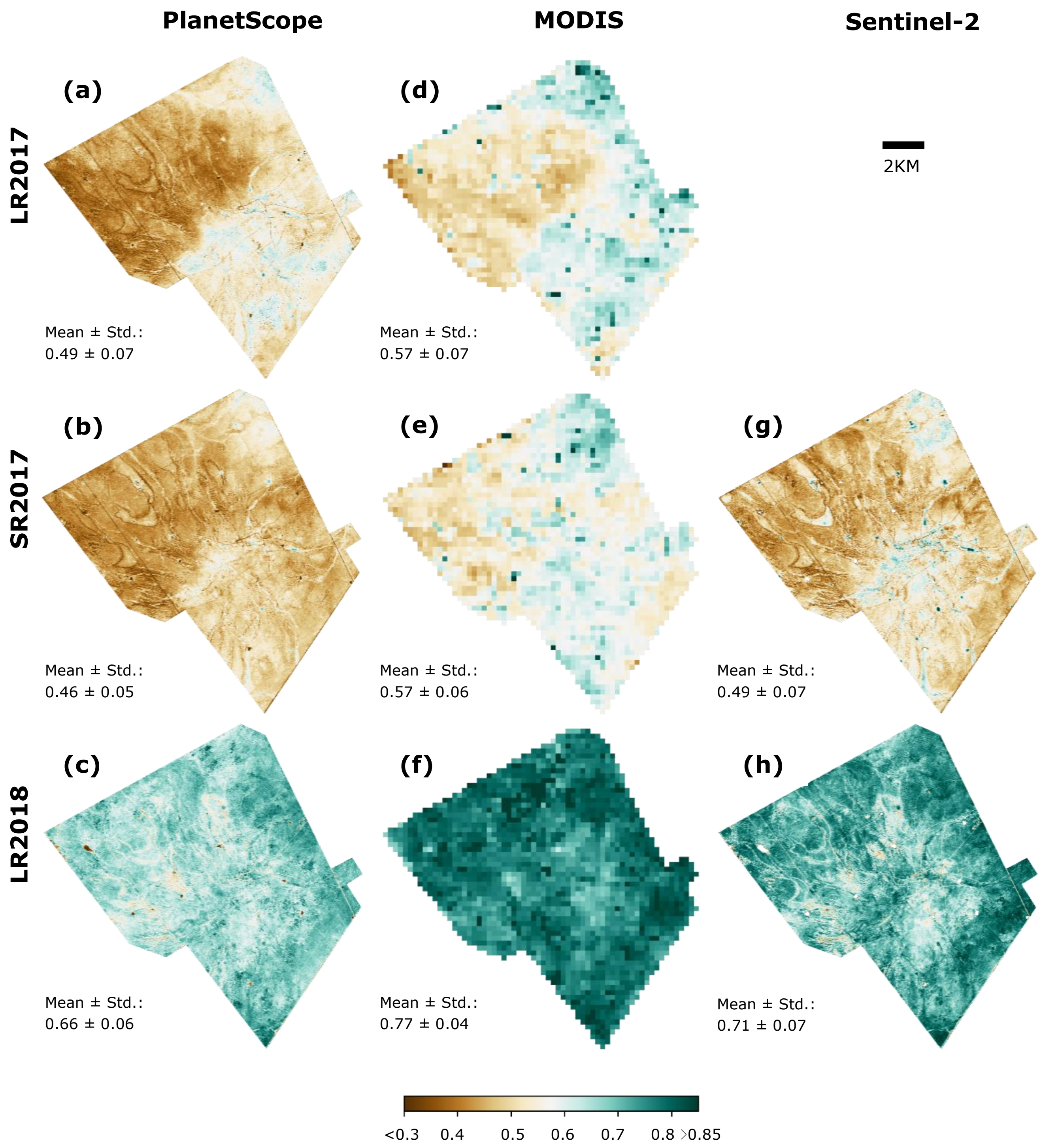

Figure A6: maxNDVI retrieved from PS, MODIS and Sentinel-2-derived NDVI time series for Kapiti Farm and per seasons. The mean and standard deviation are reported beside each map.

cumNDVI

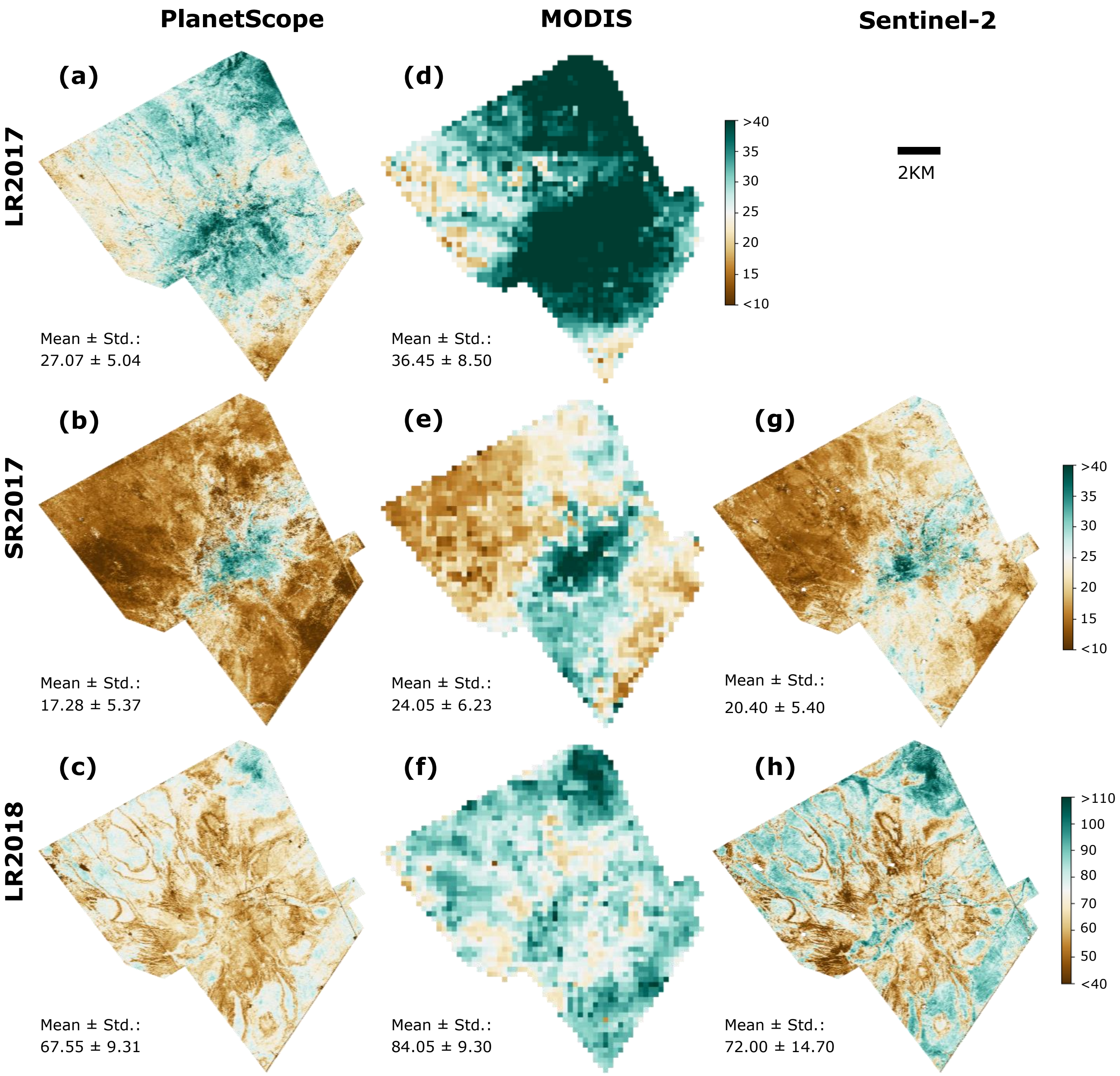

Figure A7: cumNDVI$_{50}$ retrieved from PS, MODIS and Sentinel-2-derived NDVI time series for Kapiti Farm and per seasons. The mean and standard deviation are reported beside each map. Phenology maps for each season use the same legend, which is on the left side of the map.

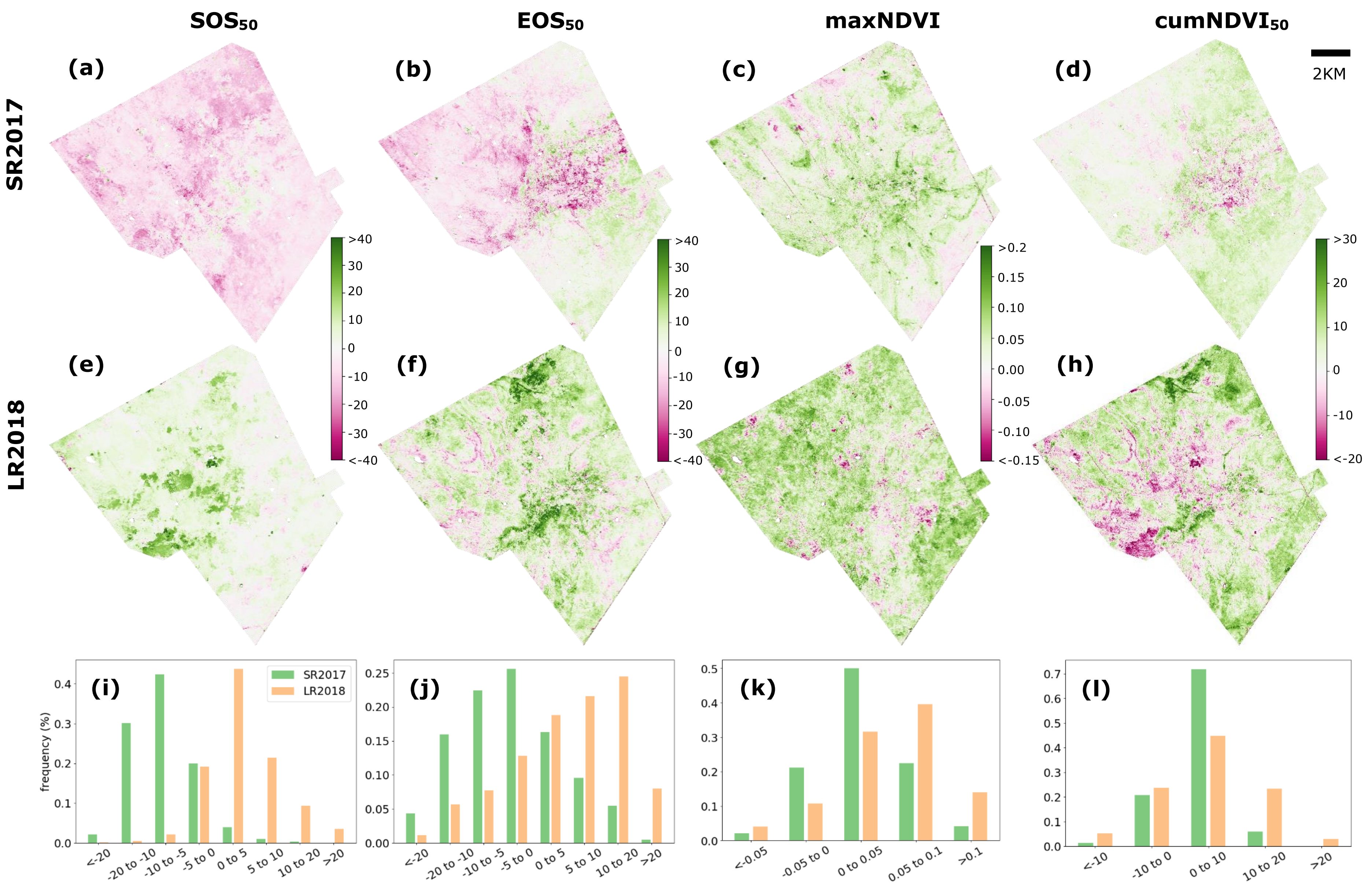

Figure A8: Difference between Sentinel-2- and PS-derived SOS_{50}, EOS_{50}, maxNDVI and $cumNDVI_{50}$. The frequency distribution of differences for four phenological metrics are shown in plot i-l.


```python

"""
Retrieving phenological metrics from NDVI time series after fitting a double hyperbolic tangent model
-----------------------------------------------------------------------------------------------------
Yan Cheng
chengyan2017@gmail.com
20/02/2019
Enschede, NL
------------

The important functions include:
1. data_initialize(basedate_, ndvi, dateRange) # clean data
2. upper_env_fit(X,X_,Y,p,imax,func, plot = None) # fit curve
3. phenoList(t,Y,t_, finalY, basedate_) # extract phenological metrics

The implementation of those functions for a specific objective:
# extract phenological metrics for one pixel
1. pheno_calc(nc_file, y, x, basedate_, dateRange, n_params, ds_QA = None, ds_DOY = None, fit = None, plot = None)
# extract phenological metrics for entire image
2. pheno_map(y_start, y_end, x_start, x_end, basedate_, dateRange, n_params, nc_file, work_dir, ds_QA = None, ds_DOY = None,
              save_arr = None, parameters = None, plot = None, save_plot = None)
Other functions:
# for visualization
draw_map(map_arr, work_dir, output_dir, file_name, extension, satellite, color_scheme = None, save_plot = None)

"""

import pandas as pd
import numpy as np

import xarray as xr
import netCDF4
from netCDF4 import Dataset

from datetime import timedelta as timedelta
from datetime import datetime
from datetime import timedelta as td
import jdcal

from scipy.optimize import leastsq
import lmfit
from lmfit import Model
from lmfit import Parameters

from scipy.integrate import simps
from scipy.stats import pearsonr
from sklearn.metrics import mean_squared_error
from math import sqrt

from multiprocessing import Pool
import pickle
import itertools
from tqdm import tqdm_notebook

import os.path
import warnings

import matplotlib.pyplot as plt
import matplotlib.cm
import matplotlib.patches as mpatches
from matplotlib.lines import Line2D
%matplotlib inline
plt.rcParams['figure.figsize'] = [7, 5]


def data_initialize(basedate_, ndvi, dateRange):

    """
    USAGE
    -----------
    - clean data
    - initialize parameter
```

Figure A9: Screenshot of python script. All python scripts written for this study were uploaded and shared through GitHub. Cloud and cloud shadow detection for PS images (https://gist.github.com/YanCheng-go/6f692136ab05e1f2345892fd0abb03dc) and Curve fitting and phenology estimation (https://gist.github.com/YanCheng-go/d4e17831f294199443d0f7682558e608).